Draft version August 30, 2022
Typeset using LaTeX default style in AASTeX63

A Comprehensive Perturbative Formalism for Phase Mixing in Perturbed Disks. II.–Phase Spirals in an Inhomogeneous Disk Galaxy with a Non-responsive Dark Matter Halo

Uddipan Banik ,[1] Frank C. van den Bosch ,[1] and Martin D. Weinberg [2]

[1]*Department of Astronomy, Yale University, PO. Box 208101, New Haven, CT 06520, USA*
[2]*Department of Astronomy, University of Massachusetts at Amherst, 710 N. Pleasant St., Amherst, MA 01003*

(Received XXX; Revised YYY; Accepted ZZZ)

ABSTRACT

Phase mixing is an essential component of the equilibration of perturbed galactic disks. We develop a linear perturbative formalism to compute the response of an inhomogeneous stellar disk embedded in a non-responsive dark matter (DM) halo to various perturbations such as bars, spiral arms and encounters with satellite galaxies. Without self-gravity to reinforce it the response of a Fourier mode phase mixes away due to an intrinsic spread in the vertical (Ω_z), radial (Ω_r) and azimuthal (Ω_ϕ) frequencies, giving rise to local phase-space spirals. The $z - v_z$ phase spiral turns out to be one-armed (two-armed) for vertically anti-symmetric (symmetric) bending (breathing) modes. Among bar and spiral arm perturbations, only transient ones that vary over timescales ($\tau_{\rm P}$) comparable to the vertical oscillation period ($\tau_z = 2\pi/\Omega_z$) can trigger vertical phase spirals. The impulsive ($\tau_{\rm P} < \tau = 1/(n\Omega_z + l\Omega_r + m\Omega_\phi)$) response for each (n, l, m) mode is power law ($\sim \tau_{\rm P}/\tau$) suppressed; the adiabatic ($\tau_{\rm P} > \tau$) response is on the other hand exponentially weak ($\sim \exp\left[-\left(\tau_{\rm P}/\tau\right)^\alpha\right]$) except resonant ($\tau \to \infty$) modes, where α is dictated by the exact time-dependence of the perturber. Slower ($\tau_{\rm P} > \tau_z$) perturbations, which for satellite galaxies correspond to more distant encounters, induce stronger bending modes. Due to the tidal distortion of the disk, the in-plane response for satellite impacts is generally dominated by the $(l, m) = (0, -2)$ mode, which resembles a two-armed warp ($n = 1$) or spiral ($n = 2$) in the $x - y$ plane. Our analysis suggests that the Solar neighborhood response of the Milky Way (MW) disk due to satellite encounters is predominantly caused by Sagittarius. Phase mixing occurs more slowly and therefore phase spirals turn out to be more loosely wound in the outer disk and in presence of an ambient DM halo. We present a novel technique to constrain the MW disk plus halo potential using the pitch angle of the phase spiral.

1. INTRODUCTION

Disk galaxies are low entropy systems characterized by large-scale ordered motion and are therefore highly responsive to perturbations. Following a time-dependent gravitational perturbation, the actions of the disk stars are modified. This in turn causes a perturbation in the distribution function (DF) of the disk known as the response. Over time the response decays away as the system 'relaxes' towards a new quasi-equilibrium via collisionless processes that include kinematic processes like phase mixing (loss of coherence in the response due to different oscillation frequencies of stars) and secular/self-gravitating/collective processes like Landau damping (loss of coherence due to wave-particle interactions, Lynden-Bell 1962). As pointed out by Sridhar (1989) and Maoz (1991), phase mixing is the key ingredient of all collisionless relaxation and re-equilibration.

The timescale of collisionless equilibration is typically longer than the orbital periods of stars. Therefore disk galaxies usually harbour prolonged features of incomplete equilibration following a perturbation, e.g., bars, spiral arms, warps and other asymmetries. An intriguing example is the one-armed phase-space spiral, or phase spiral for short, discovered in the Gaia DR2 data (Gaia Collaboration et al. 2018) by Antoja et al. (2018) and studied in more detail in subsequent studies (e.g., Bland-Hawthorn et al. 2019; Laporte et al. 2019; Li & Widrow 2021; Li 2021; Gandhi et al. 2022). Antoja

Corresponding author: Uddipan Banik
uddipan.banik@yale.edu

et al. (2018) plotted the density of stars in the Solar neighborhood in the (z, v_z)-plane of vertical position, z, and vertical velocity, v_z, and noticed a faint spiral pattern which became more pronounced when colour-coding the (z, v_z)-'pixels' by the median radial or azimuthal velocities. The one-armed spiral shows 2-3 complete wraps like a snail shell, and is interpreted as an indication of vertical phase mixing following a perturbation that is anti-symmetric about the midplane (bending mode) and occurred ~ 500 Myr ago. More recently, Hunt et al. (2022) used the more extensive Gaia DR3 data to study the distributions of stars in $z - v_z$ space at different locations in the MW disk. They found that unlike the one-armed phase spiral or bending mode at the Solar radius the inner disk shows a two-armed phase spiral that corresponds to a breathing mode or symmetric perturbation about the midplane. They inferred that while the one-armed spiral in the Solar neighborhood might have been caused by the impact of a satellite galaxy such as the Sagittarius dwarf, the two-armed spiral in the inner disk could not have been induced by the same since almost all satellite impacts are far too slow/adiabatic from the perspective of the inner disk. Rather they attributed the spiral arm as a potential triggering agent of the two-armed phase spiral.

The phase spiral holds a treasure-trove of information about the perturbative history and gravitational potential of the disk and can therefore serve as an essential tool for galactoseismology (Widrow et al. 2014; Johnston et al. 2017). For a given potential, the winding of the spiral is an indication of the time elapsed since the perturbation occurred with older spirals revealing more wraps. A one-armed (two-armed) phase spiral corresponds to a bending (breathing) mode. Which mode dominates, in turn, depends on the time-scale of the perturbation, with temporally shorter (longer) perturbations (e.g., a fast or slow encounter with a satellite) predominantly triggering breathing (bending) modes (Widrow et al. 2014; Banik et al. 2022).

In addition to depending on the nature of the perturbation, the phase spiral also encodes information about the oscillation frequencies of stars and thus the detailed potential. In particular, the shape of the spiral depends on how the vertical frequencies, Ω_z, vary as a function of the vertical action, I_z, which in turn depends on the underlying potential. Finally, the (coarse-grained) survivability of the phase spiral depends on both the spatio-temporal nature of the perturbation and the frequency structure. In Banik et al. (2022) (hereafter Paper I) we showed that non-adiabatic and spatially localized perturbations minimize the damping of the phase spiral amplitude due to lateral mixing between stars with different lateral velocities, giving rise to long-lived phase spirals.

Paper I addresses the problem of inferring the nature of the perturbation from the amplitude and structure of the phase spiral using a model of an infinite, isothermal slab for the unperturbed disk. This simple yet insightful model provides us with essential physical understanding of the perturbative response of disks without the complexity of modelling a realistic, inhomogeneous disk. However it suffers from certain glaring caveats: (i) lateral uniformity leading to an incorrect global structure of the response in the lateral direction, (ii) Maxwellian distribution of velocities in the lateral direction that overpredicts lateral mixing and consequent damping of the phase spiral amplitude, (iii) absence of dark matter (DM) halo and (iv) absence of self-gravity of the response. In this paper we relax the first three assumptions. We consider an inhomogeneous disk characterized by a realistic DF similar to the pseudo-isothermal DF (Binney 2010), that properly captures the orbital dynamics of the disk stars in 3D. In addition, we consider the effect of an underlying DM halo which for the sake of simplicity we consider to be non-responsive. This ambient DM halo alters the potential and thus the frequencies of stars, which can in turn affect the shape of the phase spiral and its coarse-grained survival. Since in this paper we are primarily interested in the phase mixing of the disk response that gives rise to phase spirals, we ignore self-gravity of the response which to linear order spawns coherent normal mode oscillations of the disk (see Mathur 1990; Weinberg 1991, for self-gravitating response of isothermal slabs).

This paper is organized as follows. Section 2 describes the standard linear perturbation theory for collisionless systems and its application to a realistic disk galaxy embedded in a DM halo that is exposed to a general perturbation. Sections 3 and 4 are concerned with computing the disk response for different perturber models. In Section 3 we compute the disk response and phase spirals for bars and spiral arms. We compute the same for encounters with satellite galaxies in Section 4. Section 5 describes how phase spirals can be used to constrain the galactic potential. We summarize our findings in Section 6.

2. LINEAR PERTURBATION THEORY FOR COLLISIONLESS SYSTEMS

2.1. *Linear perturbative formalism*

Let the unperturbed steady state Hamiltonian of a collisionless stellar system be H_0 and the corresponding DF be given by f_0, which satisfies the CBE,

$$[f_0, H_0] = 0. \tag{1}$$

Here the square brackets denote the Poisson bracket. In presence of a small time-dependent perturbation in the potential, $\Phi_{\rm P}(t)$, the perturbed Hamiltonian can be written as

$$H = H_0 + \Phi_{\rm P}(t) + \Phi_1(t), \tag{2}$$

where Φ_1 is the gravitational potential related to the response density, $\rho_1 = \int f_1 {\rm d}^3\mathbf{v}$, via the Poisson equation,

$$\nabla^2 \Phi_1 = 4\pi G \rho_1. \tag{3}$$

The perturbed DF can be written as

$$f = f_0 + f_1, \tag{4}$$

where f_1 is the linear order perturbation in the DF. In the weak perturbation limit where linear perturbation theory holds, the time-evolution of f_1 is dictated by the following linearized form of the CBE:

$$\frac{\partial f_1}{\partial t} + [f_1, H_0] + [f_0, \Phi_{\rm P}] + [f_0, \Phi_1] = 0. \tag{5}$$

Throughout this paper we neglect the self-gravity of the disk, which implies that we set the polarization term, $[f_0, \Phi_1] = 0$. The implications of including self-gravity are discussed in Paper I.

2.2. *Response of a Galactic Disk to a realistic perturbation*

The dynamics of a realistic disk galaxy like the Milky Way (MW) is quasi-periodic, i.e., can be characterized by oscillations in the azimuthal, radial and vertical directions. In close proximity to the mid-plane, the potential of the unperturbed galactic disk can be approximated by a separable function of the galactocentric radius, R, and the vertical distance, z. Thus the Hamilton-Jacobi equation also becomes separable, implying that all stars confined within a few vertical scale heights from the mid-plane of the disk are on regular, quasi-periodic orbits that are characterized by a radial action, I_R, an azimuthal action I_ϕ, and a vertical action I_z. Hence, the motion of each star is characterized by three frequencies:

$$\Omega_R = \frac{\partial H_0}{\partial I_R}\,, \quad \Omega_\phi = \frac{\partial H_0}{\partial I_\phi}\,, \quad \Omega_z = \frac{\partial H_0}{\partial I_z}\,. \tag{6}$$

This quasi-periodic nature of the orbits near the mid-plane is approximately preserved even in presence of a DM halo. However, the halo deepens the overall potential increasing the frequencies of the disk stars.

In terms of these canonically conjugate action-angle variables, the linearized form of the CBE given in Equation (5) becomes

$$\frac{\partial f_1}{\partial t} + \frac{\partial H_0}{\partial I_z}\frac{\partial f_1}{\partial w_z} + \frac{\partial H_0}{\partial I_R}\frac{\partial f_1}{\partial w_R} + \frac{\partial H_0}{\partial I_\phi}\frac{\partial f_1}{\partial w_\phi} - \frac{\partial \Phi_{\rm P}}{\partial w_z}\frac{\partial f_0}{\partial I_z} - \frac{\partial \Phi_{\rm P}}{\partial w_R}\frac{\partial f_0}{\partial I_R} - \frac{\partial \Phi_{\rm P}}{\partial w_\phi}\frac{\partial f_0}{\partial I_\phi} = 0. \tag{7}$$

Since the stars move along quasi-periodic orbits characterized by actions and angles, we can expand the perturbations, $\Phi_{\rm P}$ and f_1, as discrete Fourier series in the angles as follows

$$\begin{aligned}
\Phi_{\rm P}\left(\mathbf{w}, \mathbf{I}, t\right) &= \sum_{n=-\infty}^{\infty}\sum_{l=-\infty}^{\infty}\sum_{m=-\infty}^{\infty} \exp\left[i(nw_z + lw_R + mw_\phi)\right]\Phi_{nlm}\left(\mathbf{I}, t\right), \\
f_1\left(\mathbf{w}, \mathbf{I}, t\right) &= \sum_{n=-\infty}^{\infty}\sum_{l=-\infty}^{\infty}\sum_{m=-\infty}^{\infty} \exp\left[i(nw_z + lw_R + mw_\phi)\right] f_{1nlm}(\mathbf{I}, t),
\end{aligned} \tag{8}$$

where $\mathbf{w} = (w_z, w_R, w_\phi)$ and $\mathbf{I} = (I_z, I_R, I_\phi)$. Substituting these Fourier expansions in equation (7) yields the following differential equation for the evolution of f_{1nlm}:

$$\frac{\partial f_{1nlm}}{\partial t} + i(n\Omega_z + l\Omega_R + m\Omega_\phi) f_{1nlm} = i\left(n\frac{\partial f_0}{\partial I_z} + l\frac{\partial f_0}{\partial I_R} + m\frac{\partial f_0}{\partial I_\phi}\right)\Phi_{nlm}. \tag{9}$$

This can be solved using the Green's function technique, with the initial condition, $f_{1nlm}(t_\mathrm{i}) = 0$, to yield the following closed integral form for f_{1nlm}:

$$f_{1nlm}(\mathbf{I}, t) = i\left(n\frac{\partial f_0}{\partial I_z} + l\frac{\partial f_0}{\partial I_R} + m\frac{\partial f_0}{\partial I_\phi}\right)\int_{t_\mathrm{i}}^{t} \mathrm{d}\tau \exp\left[-i(n\Omega_z + l\Omega_R + m\Omega_\phi)(t-\tau)\right]\Phi_{nlm}(\mathbf{I}, \tau). \tag{10}$$

The (n, l, m) Fourier mode of every star or phase-space element acts as a forced oscillator with three different natural frequencies, $n\Omega_z$, $l\Omega_R$ and $m\Omega_\phi$, which is being driven by an external time-dependent perturber potential, Φ_{nlm}. A similar expression for the DF perturbation has been derived by Carlberg & Sellwood (1985) in the context of spiral arm induced perturbations and radial migrations in the galactic disk, and by other previous studies (e.g., Lynden-Bell & Kalnajs 1972; Tremaine & Weinberg 1984; Carlberg & Sellwood 1985; Weinberg 1989, 1991, 2004; Kaur & Sridhar 2018; Banik & van den Bosch 2021a; Kaur & Stone 2022) in the context of dynamical friction in spherical systems. To obtain the final expression for f_{1nlm}, we need to specify the DF f_0 of the unperturbed galaxy, as well as the spatio-temporal behavior of the perturber potential, Φ_P, which is addressed below.

2.3. *The unperturbed galaxy*

Under the radial epicyclic approximation (small I_R), the unperturbed DF, f_0, for a rotating MW-like disk galaxy can be well approximated as a pseudo-isothermal DF, i.e., written as a nearly isothermal separable function of the azimuthal, radial and vertical actions. Following Binney (2010), we write

$$f_0 = \frac{1}{\pi}\left(\frac{\Omega_\phi \Sigma}{\kappa\,\sigma_R^2}\right)_{R_\mathrm{c}}\left(1 + \tanh\frac{L_z}{L_0}\right) \times \exp\left[-\frac{\kappa I_R}{\sigma_R^2}\right] \times \frac{1}{\sqrt{2\pi} h_z \sigma_z}\exp\left[-\frac{E_z(I_z)}{\sigma_z^2}\right]. \tag{11}$$

The vertical structure of this disk is isothermal, while the radial profile is pseudo-isothermal. Here $\Sigma = \Sigma(R)$ is the surface density of the disk. L_z is the z-component of the angular momentum, which is equal to I_ϕ, $R_\mathrm{c} = R_\mathrm{c}(L_z)$ is the guiding radius, Ω_ϕ is the circular frequency and $\kappa = \kappa(R_c) = \lim_{I_R \to 0}\Omega_R$ is the radial epicyclic frequency (Binney & Tremaine 1987). If L_0 is sufficiently small, then we can further approximate the above form for f_0 as

$$f_0 \approx \frac{\sqrt{2}}{\pi^{3/2}\,\sigma_z h_z}\left(\frac{\Omega_\phi \Sigma}{\kappa\,\sigma_R^2}\right)_{R_c} \exp\left[-\frac{\kappa I_R}{\sigma_R^2}\right]\exp\left[-\frac{E_z(I_z)}{\sigma_z^2}\right]\Theta(L_z)\,, \tag{12}$$

where $\Theta(x)$ is the Heaviside step function. Thus we assume that the entire galaxy is composed of prograde stars with $L_z > 0$.

The corresponding density profile can be written as a product of an exponential radial profile and an isothermal (sech^2) vertical profile, i.e.,

$$\rho(R, z) = \rho_\mathrm{c}\,\exp\left[-\frac{R}{h_R}\right]\mathrm{sech}^2\left(\frac{z}{h_z}\right), \tag{13}$$

where h_R and h_z are the radial and vertical scale heights respectively. Throughout we adopt the thin disk limit, i.e., $h_z \ll h_R$. The surface density profile is given by

$$\Sigma(R) = \int_{-\infty}^{\infty}\mathrm{d}z\,\rho(R, z) = \Sigma_\mathrm{c}\exp\left[-\frac{R}{h_R}\right], \tag{14}$$

where $\Sigma_\mathrm{c} = \rho_\mathrm{c} h_z$ is the central surface density of the disk. The above density profile can be approximated by a combination of three Miyamoto & Nagai (1975) disk profiles (Smith et al. 2015), i.e., the 3MN profile as implemented in the `Gala` Python package (Price-Whelan 2017; Price-Whelan et al. 2020). The corresponding disk potential is given by

$$\Phi_\mathrm{d}(R, z) = -\sum_{i=1}^{3}\frac{GM_i}{\sqrt{R^2 + \left(a_i + \sqrt{z^2 + b_i^2}\right)^2}}, \tag{15}$$

where M_i, a_i and b_i, with $i = 1, 2, 3$, are the mass, scale radius and scale height corresponding to each of the MN profiles. Throughout we use the 3MN potential to compute the frequencies of the disk stars.

The MW disk is believed to be embedded in a much more extended DM halo, which we model using a spherical NFW (Navarro et al. 1997) profile with potential

$$\Phi_{\rm h}(R,z) = -\frac{GM_{\rm vir}}{f(c)}\frac{1}{\sqrt{R^2+z^2}}\ln\left(1+\frac{\sqrt{R^2+z^2}}{r_{\rm h}}\right). \tag{16}$$

Here $M_{\rm vir}$ is the virial mass of the halo, r_h is the scale radius, $c = R_{\rm vir}/r_{\rm h}$ is the concentration ($R_{\rm vir}$ is the virial radius), and $f(c) = \ln(1+c) - c/(1+c)$. The combined potential experienced by the disk stars is thus given by

$$\Phi_0(R,z) = \Phi_{\rm d}(R,z) + \Phi_{\rm h}(R,z). \tag{17}$$

The total energy of a disk star under the radial epicyclic approximation is $E = \Omega_\phi L_z + \kappa I_R + E_z$, where the vertical part of the energy is given by $E_z = v_z^2/2 + \Phi_z(R_c, z)$, with $R_c(L_z)$ the guiding radius given by $L_z^2/R_c^3 = \partial\Phi_0/\partial R|_{R=R_c}$. The vertical potential, $\Phi_z(R_c, z)$, is given by

$$\Phi_z(R_c,z) = \Phi_0(R_c,z) - \Phi_0(R_c,0). \tag{18}$$

As discussed above, the vertical (radial) density profile is well described by the isothermal sech^2 (exponential) profile in the solar neighborhood. Thus, near the sun, $\Phi_z(R,z) \approx 2\,\sigma_z^2(R)\ln[\cosh(z/h_z)]$ and $\Phi_{\rm d}(R,0) \approx \pi G\Sigma_{\rm c} h_R\,[I_1(R/2h_R)\,K_0(R/2h_R) - I_0(R/2h_R)\,K_1(R/2h_R)]$, where I_n and K_n are modified Bessel functions of the first and second kind, respectively.

The vertical action, I_z, can be obtained from the unperturbed energy, E_z, as follows

$$I_z = \frac{1}{2\pi}\oint v_z\,dz = \frac{2}{\pi}\int_0^{z_{\max}}\sqrt{2[E_z-\Phi_z(R_c,z)]}\,dz, \tag{19}$$

where $\Phi_z(R_c, z_{\max}) = E_z$. This implicit equation can be inverted to obtain $E_z(R_c, I_z)$. The time period of vertical oscillation can then be obtained using

$$T_z(R_c,I_z) = \oint\frac{dz}{v_z} = 4\int_0^{z_{\max}}\frac{dz}{\sqrt{2\,[E_z(R_c,I_z)-\Phi_z(R_c,z)]}}, \tag{20}$$

which yields the vertical frequency, $\Omega_z(R_c, I_z) = 2\pi/T_z(R_c, I_z)$.

We assume a radially varying vertical velocity dispersion, σ_z, satisfying (Binney & Tremaine 2008)

$$\sigma_z^2(R) = 2\pi G h_z \Sigma(R). \tag{21}$$

We also assume a similar exponential profile for σ_R^2 such that the ratio, σ_R/σ_z is constant throughout the disk (Binney 2010) and equal to the value at the solar vicinity.

Throughout, for the purpose of computing the disk response, we assume typical MW like parameters for the various quantities, i.e., $R_\odot = 8$ kpc, disk mass $M_{\rm d} = 5\times10^{10}\,{\rm M}_\odot$, $h_R = 2.2$ kpc, $\sigma_R(R_\odot) = 35$ km/s, $h_z = 0.4$ kpc (McMillan 2011; Bovy & Rix 2013). For the NFW DM halo, we adopt $M_{\rm vir} = 9.78\times10^{11}\,{\rm M}_\odot$, $r_{\rm h} = 16$ kpc, and $c = 15.3$ (Bovy 2015).

Substituting the expression for f_0 given by Equation (12) in Equation (10), we obtain the following integral form for f_{1nlm},

$$f_{1nlm}(\mathbf{I},t) \approx -\frac{2i}{\pi\sigma_R^2}\frac{1}{\sqrt{2\pi}h_z\sigma_z}\left[\left\{\left(\frac{n\Omega_z}{\sigma_z^2}+\frac{l\kappa}{\sigma_R^2}\right)\left(\frac{\Omega_\phi\Sigma}{\kappa}\right) - m\frac{\mathrm{d}}{\mathrm{d}L_z}\left(\frac{\Omega_\phi\Sigma}{\kappa}\right)\right\}\Theta(L_z) - m\frac{\Omega_\phi\Sigma}{\kappa}\delta(L_z)\right]$$

$$\times\exp\left[-\frac{\kappa I_R}{\sigma_R^2}\right]\exp\left[-\frac{E_z(I_z)}{\sigma_z^2}\right]\int_{t_{\rm i}}^{t}\mathrm{d}\tau\,\exp\left[-i(n\Omega_z+l\kappa+m\Omega_\phi)(t-\tau)\right]\Phi_{nlm}(\mathbf{I},\tau). \tag{22}$$

As we shall see, the first order disk response expressed above phase mixes away and gives rise to phase spirals due to oscillations of stars with different frequencies except when they are resonant with the frequency of the perturber.

However this 'direct' response of the disk does not include certain effects. First of all, we ignore the self-gravity of the response. As discussed in Paper I, to linear order self-gravity gives rise to normal mode oscillations of the disk that are decoupled from the phase mixing component of the response which is what we are interested in. Secondly, for the sake of simplicity, we consider the ambient DM halo to be non-responsive and therefore ignore the indirect effect of the halo response on disk oscillations. We leave the inclusion of these two effects in the computation of the disk response for future work.

The spatio-temporal nature of the perturbing potential dictates the disk response. In this paper we explore two different types of perturbation to which realistic disc galaxies can be exposed, and which are thus of general astrophysical interest. The first is an in-plane spiral/bar perturbation with a vertical structure, either formed as a consequence of secular evolution, or triggered by an external perturbation. We will consider both short-lived (transient) and persistent spirals. The second type of perturbation that we consider is that due to an encounter with a massive object, e.g., a satellite galaxy or DM subhalo.

3. DISK RESPONSE TO SPIRAL ARMS AND BARS

We model the potential of a spiral arm perturbation as one with a vertical profile and a sinusoidal variation along radial and azimuthal directions,

$$\Phi_{\mathrm{P}}(R,\phi,z) = -\frac{2\pi G\Sigma_{\mathrm{P}}}{k_R}\left[\alpha\,\mathcal{M}_{\mathrm{o}}(t)\,\mathcal{F}_{\mathrm{o}}(z) + \mathcal{M}_{\mathrm{e}}(t)\,\mathcal{F}_{\mathrm{e}}(z)\right]\sum_{m_\phi=0,2}\sin\left[k_R R + m_\phi\left(\phi - \Omega_{\mathrm{P}} t\right)\right]. \tag{23}$$

Here Ω_{P} is the pattern speed and k_R is the horizontal wave number of the spiral perturbation. The long wavelength limit, $k_R \to 0$, corresponds to a bar. We consider the in-plane part of Φ_{P} to be a combination of an axisymmetric ($m_\phi = 0$) and a 2-armed spiral mode ($m_\phi = 2$), and the vertical part to be a combination of anti-symmetric/odd and symmetric/even perturbations respectively denoted by $\mathcal{F}_{\mathrm{o}}$ and $\mathcal{F}_{\mathrm{e}}$, that differ by the ratio α and are modulated by growth functions, $\mathcal{M}_{\mathrm{o}}(t)$ and $\mathcal{M}_{\mathrm{e}}(t)$, that capture the growth and/or decay of the spiral strength over time. We consider the following two functional forms for $\mathcal{M}_j(t)$ (where the subscript $j = $ o or e):

$$\mathcal{M}_j(t) = \begin{cases} \frac{1}{\sqrt{\pi}}\exp\left[-\omega_j^2 t^2\right], & \text{Transient spiral/bar} \\ \exp\left[\gamma_j t\right] + \left(1 - \exp\left[\gamma_j t\right]\right)\,\Theta(t), & \text{Persistent spiral/bar.} \end{cases} \tag{24}$$

The first option describes a transient spiral/bar that grows and decays like a Gaussian pulse with a characteristic lifetime $\tau_{\mathrm{P}j} \sim 1/\omega_j$. The second form describes a persistent spiral perturbation that grows exponentially on a timescale $\tau_{\mathrm{G}j} \sim 1/\gamma_j$ and then saturates to a constant amplitude. We shall see shortly that these two kinds of spiral perturbations perturb the disk in very different ways.

The vertical part of the perturbation consists of an anti-symmetric function, $\mathcal{F}_{\mathrm{o}}(z)$, and a symmetric function, $\mathcal{F}_{\mathrm{e}}(z)$, which, for the sake of simplicity, we take to be the following trigonometric functions:

$$\begin{aligned}\mathcal{F}_{\mathrm{o}}(z) &= \sin\left(k_z^{(\mathrm{o})} z\right),\\ \mathcal{F}_{\mathrm{e}}(z) &= \cos\left(k_z^{(\mathrm{e})} z\right).\end{aligned} \tag{25}$$

Here $k_z^{(\mathrm{o})}$ and $k_z^{(\mathrm{e})}$ denote the vertical wave-numbers of the anti-symmetric and symmetric perturbations, respectively. Since the above functions form a complete Fourier basis in z, any (vertical) perturber profile can be expressed as a linear superposition of $\mathcal{F}_{\mathrm{o}}$ and $\mathcal{F}_{\mathrm{e}}$.

To compute the disk response, we need to compute the Fourier coefficients of the perturbing potential, Φ_{nlm}, which can be obtained by taking the Fourier transform of Φ_{P} given in Equation (23) with respect to the angles, w_R, w_ϕ and w_z. As detailed in Appendix A this yields:

$$\begin{aligned}\Phi_{nlm}\left(\mathbf{I},t\right) = &-\frac{2\pi G\Sigma_{\mathrm{P}}}{k_R}\left(\sum_{m_\phi=0,2,-2}\delta_{m,m_\phi}\right)\frac{\mathrm{sgn}(m)\exp\left[i\,\mathrm{sgn}(m)k_R R_c(I_\phi)\right]}{2i}\,J_l\left(k_R\sqrt{\frac{2I_R}{\kappa}}\right)\\ &\times\left[\alpha\,\mathcal{M}_{\mathrm{o}}(t)\Phi_n^{(\mathrm{o})}(I_z) + \mathcal{M}_{\mathrm{e}}(t)\Phi_n^{(\mathrm{e})}(I_z)\right]\exp\left[-im\Omega_{\mathrm{P}} t\right],\end{aligned} \tag{26}$$

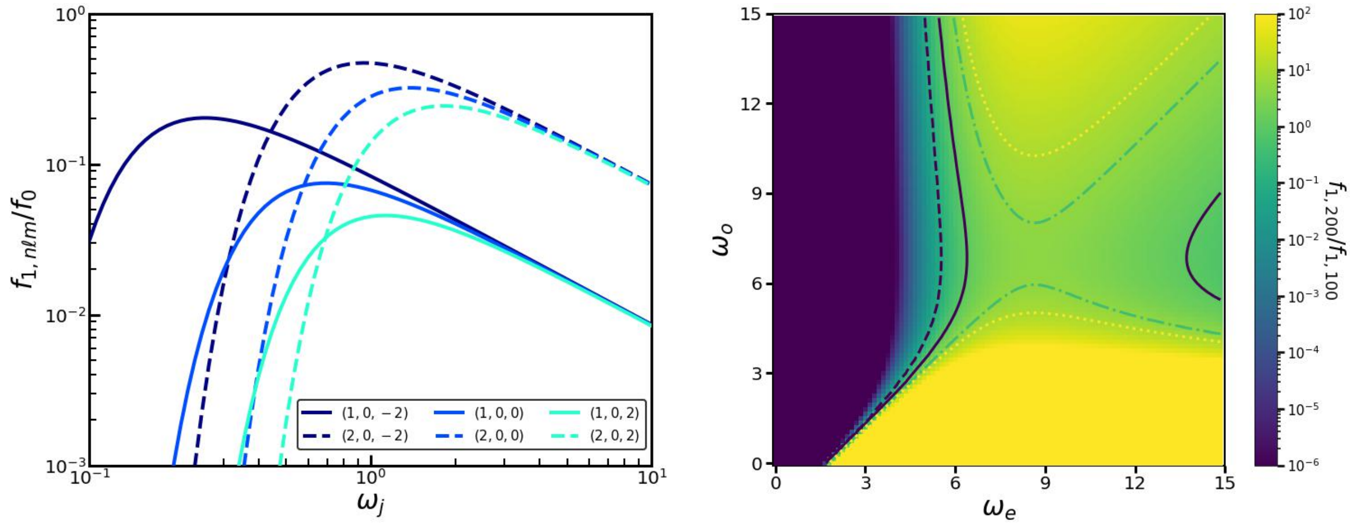

Figure 1: MW disk response to transient bars/2-armed spirals with Gaussian temporal modulation: Left panel shows the amplitude of the disk response, $f_{1,nlm}/f_0$, in the Solar neighborhood, computed using equations (29) and (32) in presence of an ambient DM halo, as a function of the pulse frequency, ω_j, where the subscript $j = \mathrm{o}$ and e for vertically anti-symmetric (odd n) and symmetric (even n) perturbations. Solid (dashed) lines indicate the $n = 1$ bending ($n = 2$ breathing) modes and different colors denote $(l, m) = (0, -2)$, $(0, 0)$ and $(0, 2)$ respectively. Note that the response peaks at intermediate values of ω_j, which is different for different modes, and is suppressed like a power law in the impulsive (large ω_j) limit and super-exponentially in the adiabatic (small ω_j) limit. Right panel shows the breathing-to-bending ratio, $f_{1,200}/f_{1,100}$, as a function of ω_e and ω_o, the pulse frequencies of the bending and breathing mode perturbations respectively. The dashed, solid, dot-dashed and dotted contours correspond to breathing-to-bending ratios of $0.1, 1, 5$ and 10 respectively. The breathing-to-bending ratio rises and falls with increasing ω_e at fixed ω_o, while the reverse occurs with increasing ω_o at fixed ω_e, leading to a saddle point at $(\omega_\mathrm{e}, \omega_\mathrm{o}) \approx (9, 7)$.

where J_l is the l^{th} order Bessel function of the first kind and

$$\mathrm{sgn}(m) = \begin{cases} 1, & m \geq 0, \\ -1, & m < 0. \end{cases} \tag{27}$$

The functions $\Phi_n^{(\mathrm{o})}(I_z)$ and $\Phi_n^{(\mathrm{e})}(I_z)$ are given by

$$\begin{aligned} \Phi_n^{(\mathrm{o})}(I_z) &= \frac{1}{2\pi} \int_0^{2\pi} \mathrm{d}w_z \sin nw_z \, \mathcal{F}_\mathrm{o}\left(z, k_z^{(\mathrm{o})}\right), \\ \Phi_n^{(\mathrm{e})}(I_z) &= \frac{1}{2\pi} \int_0^{2\pi} \mathrm{d}w_z \cos nw_z \, \mathcal{F}_\mathrm{e}\left(z, k_z^{(\mathrm{e})}\right). \end{aligned} \tag{28}$$

3.1. *Computing the disk response*

The expression for the disk response to bars or spiral arms can be obtained by substituting the Fourier coefficient of the perturber potential given in Equation (26) in Equation (22) and performing the τ integration with the initial time, $t_\mathrm{i} \to -\infty$. This yields

$$\begin{aligned} f_1(\mathbf{w}, \mathbf{I}, t) = &-\frac{2i}{\pi\sigma_R^2} \frac{1}{\sqrt{2\pi} h_z \sigma_z} \exp\left[-\frac{\kappa I_R}{\sigma_R^2}\right] \exp\left[-\frac{E_z(I_z)}{\sigma_z^2}\right] \\ &\times \sum_{n,l,m=-\infty}^{\infty} \left[\left(\frac{n\Omega_z}{\sigma_z^2} + \frac{l\kappa}{\sigma_R^2}\right)\left(\frac{\Omega_\phi \Sigma}{\kappa}\right) - m\frac{\mathrm{d}}{\mathrm{d}L_z}\left(\frac{\Omega_\phi \Sigma}{\kappa}\right)\right] \left[\alpha \, \Psi_{nlm}^{(\mathrm{o})} \, \mathcal{P}_{nlm}^{(\mathrm{o})}(t) + \Psi_{nlm}^{(\mathrm{e})} \, \mathcal{P}_{nlm}^{(\mathrm{e})}(t)\right] \exp\left[i\left(nw_z + lw_R + mw_\phi\right)\right], \end{aligned} \tag{29}$$

where $\Psi^{(\mathrm{o})}_{nlm}$ and $\Psi^{(\mathrm{e})}_{nlm}$ respectively denote the time-independent parts of the odd and even terms in the expression for Φ_{nlm}. The temporal modulation and oscillation terms of Φ_{P} are integrated over τ to yield

$$\mathcal{P}^{(j)}_{nlm}(t) = \exp\left[-i\,\Omega_{\mathrm{P}}\,t\right]\int_0^\infty \mathrm{d}\tau \exp\left[-i\,\Omega_{\mathrm{res}}\,\tau\right]\mathcal{M}_j(t-\tau) \tag{30}$$

with the resonance frequency, Ω_{res}, given by

$$\Omega_{\mathrm{res}} = n\Omega_z + l\kappa + m(\Omega_\phi - \Omega_{\mathrm{P}}). \tag{31}$$

3.1.1. *Transient spirals and bars*

First we consider the case of transient spiral arm or bar perturbations that grow and decay in strength over time, i.e., the temporal modulation $\mathcal{M}_j(t)$ is given by the first of equations (24). In this case,

$$\begin{aligned}\mathcal{P}^{(j)}_{nlm}(t) &= \frac{1}{2\,\omega_j}\,\exp\left[-\frac{\Omega^2_{\mathrm{res}}}{4\omega_j^2}\right]\left[1+\mathrm{erf}\left(\omega_j t - i\frac{\Omega_{\mathrm{res}}}{2\omega_j}\right)\right]\exp\left[-i(n\Omega_z + l\kappa + m\Omega_\phi)t\right] \\ &\xrightarrow{t\to\infty} \frac{1}{\omega_j}\,\exp\left[-\frac{\Omega^2_{\mathrm{res}}}{4\omega_j^2}\right]\exp\left[-i(n\Omega_z + l\kappa + m\Omega_\phi)t\right].\end{aligned} \tag{32}$$

The left-hand panel of Fig. 1 plots the disk response to transient spiral/bar perturbations as a function of the modulation/pulse frequency, ω_j (j = o and e for bending and breathing modes respectively), for different modes indicated in different colors. Solid and dashed lines correspond to the $n=1$ bending modes and the $n=2$ breathing modes, respectively. We adopt $\Sigma_{\mathrm{P}} = 5.5\,\mathrm{M_\odot\,pc^{-2}}$, $\Omega_{\mathrm{P}} = 12\ \mathrm{km}s^{-1}\,\mathrm{kpc}^{-1}$, $k_z^{(o)} = k_z^{(e)} = 1\,\mathrm{kpc}$, and $k_R = 10\,\mathrm{kpc}$. We set $\alpha = 1$, implying equal maximum strengths for the bending and breathing modes. As evident from this figure, and also from equation (32), the long-term strength of the disk response (after the initial transients have died out like $e^{-\omega_j^2 t^2}$) scales as $\sim 1/\omega_j$ in the impulsive (large ω_j) limit, but is super-exponentially suppressed ($\sim \exp\left[-\Omega^2_{\mathrm{res}}/4\omega_j^2\right]$) in the adiabatic (small ω_j) limit, except at the resonances, $\Omega_{\mathrm{res}} = 0$, for which the response scales as $\sim 1/\omega_j$ throughout and becomes non-linear in the adiabatic regime. The adiabatic suppression scales differently with ω_j for other functional forms of $\mathcal{M}_j(t)$, e.g., for $\mathcal{M}_j(t) = 1/\sqrt{1+\omega_j^2 t^2}$ the response strength is exponentially suppressed ($\sim \exp\left[-\Omega_{\mathrm{res}}/\omega_j\right]$).

The sinusoidal factor, $\exp\left[-i(n\Omega_z + l\kappa + m\Omega_\phi)t\right]$, in $\mathcal{P}^{(j)}_{nlm}(t)$ describes the oscillations of stars with three different frequencies, Ω_z, κ and Ω_ϕ, along the vertical, radial and azimuthal directions, respectively. Due to the dependence of these frequencies on the actions, that of Ω_z on I_z and of κ and Ω_ϕ on $I_\phi = L_z$, the response eventually phase mixes away. This manifests as phase spirals in the $I_z \cos w_z - I_z \sin w_z$ and $I_\phi \cos\phi - I_\phi \sin\phi$ phase-spaces, which are proxies for the $z - v_z$ and $\phi - \dot{\phi}$ phase-spaces, respectively. As shown in Paper I, $n=1$ bending modes involve a dipolar perturbation in the vertical phase-space ($I_z \cos w_z - I_z \sin w_z$) distribution immediately after the perturbing pulse reaches its maximum strength. This dipolar distortion is subsequently wound up into a one-armed phase spiral since Ω_z is a function of I_z. Breathing modes, on the other hand, involve an initial quadrupolar perturbation in the phase-space distribution which is subsequently wrapped up into a two-armed phase spiral. Since Ω_z, Ω_ϕ and Ω_R all depend on L_z, the amplitude of the $I_z \cos w_z - I_z \sin w_z$ phase spiral damps out over time due to mixing between stars with different L_z, typically as $\sim 1/t$. This explains why the density-contrast of the Gaia phase spiral is enhanced upon color-coding by v_ϕ or, equivalently, L_z (Antoja et al. 2018; Bland-Hawthorn et al. 2019). Radial phase mixing is also present, but is typically much weaker because none of the frequencies depend on I_R under the radial epicyclic approximation and only mildly depend on I_R without it. Hence, due to ordered motion, the phase spiral in a realistic disk galaxy damps out at a much slower rate than the lateral mixing damping (temporally Gaussian for laterally plane wave perturbation) in the isothermal slab case considered in Paper I, which arises from the unconstrained lateral velocities of the stars.

It is worth emphasizing that not all frequencies undergo phase mixing. In fact the resonant frequencies, for which

$$\Omega_{\mathrm{res}} = n\Omega_z + l\kappa + m(\Omega_\phi - \Omega_{\mathrm{P}}) = 0, \tag{33}$$

do not phase mix away. Hence, the near-resonant parts of phase-space undergo gradual phase mixing. Moreover, as manifest from the adiabatic suppression factor, $\exp[-\Omega^2_{\mathrm{res}}/4\omega_0^2]$, the near-resonant modes with $\Omega_{\mathrm{res}} \ll 2\omega_0$ have much larger amplitude than those with $\Omega_{\mathrm{res}} \gg 2\omega_0$ that are far from resonance. Therefore the long-term disk response consists of stars in (near) resonance with the perturbing bar or spiral arm. Most of the strong resonances are confined to the disk-plane, including the co-rotation resonance $(n, l, m) = (0, 0, m)$, the Lindblad resonances $(0, \pm 1, \pm 2)$, the ultraharmonic resonances $(0, \pm 1, \pm 4)$, and so on. For thin disks with $h_z \ll h_R$, the vertical degrees of freedom are generally not in resonance with the radial or azimuthal ones since Ω_z is much larger than Ω_ϕ or κ. Hence the vertical oscillation modes $(n \neq 0)$ such as the $n = 1$ bending or $n = 2$ breathing modes undergo phase mixing and give rise to phase spirals.

The excitability of the bending and breathing modes is dictated by the perturbation timescale, or more precisely by the ratio of the pulse frequency, ω_j, and the resonant frequency, Ω_{res}. The right panel of Fig. 1 shows the breathing-to-bending ratio, $f_{1,200}/f_{1,100}$, as a function of ω_{e} and ω_{o}, with blue (yellow) shades indicating low (high) values. In general, the breathing-to-bending ratio rises steeply and falls gradually with ω_{e} at fixed ω_{o} while the trend is reversed as a function of ω_{o} at fixed ω_{e}, resulting in a saddle point at $(\omega_{\mathrm{e}}, \omega_{\mathrm{o}}) \approx (9, 7)$. This owes to the super-exponential suppression in the adiabatic $(\omega_j \ll \Omega_{\mathrm{res}})$ limit and the power-law suppression in the impulsive $(\omega_j \gg \Omega_{\mathrm{res}})$ limit. Along the $\omega_{\mathrm{o}} = \omega_{\mathrm{e}}$ line, the bending (breathing) modes dominate in the adiabatic (impulsive) limit, as evident from the left panel of Fig. 1. All this suggests that bending (breathing) modes dominate over breathing (bending) modes when (i) the anti-symmetric (symmetric) perturbation is more impulsive, i.e., evolves faster than the symmetric (anti-symmetric) one, and (ii) both symmetric and anti-symmetric perturbations occur over comparable timescales but slower (faster) than the stellar vertical oscillation period.

3.1.2. *Persistent spirals and bars*

Next we consider perturbations caused by a persistent spiral arm or bar that grows exponentially until it saturates at a constant strength. The corresponding temporal modulation $\mathcal{M}_j(t)$ is given by the second of equations (24). In this case, as shown by equation (19) of Banik & van den Bosch (2021a),

$$\mathcal{P}^{(j)}_{nlm}(t) = \frac{\exp\left[\gamma_j t\right] \exp\left[-im\Omega_{\mathrm{P}} t\right]}{\gamma_j + i\Omega_{\mathrm{res}}} \left[1 - \theta(t)\right] + i \left[\frac{\gamma_j \exp\left[-i(n\Omega_z + l\kappa + m\Omega_\phi)t\right]}{\Omega_{\mathrm{res}}(\gamma_j + i\Omega_{\mathrm{res}})} - \frac{\exp\left[-im\Omega_{\mathrm{P}} t\right]}{\Omega_{\mathrm{res}}}\right] \theta(t). \tag{34}$$

Up to $t = 0$ when the perturber amplitude stops growing, the response from all modes oscillates with the pattern speed Ω_{P} and grows hand in hand with the perturber. Subsequently, as the perturbation attains a steady strength, the disk response undergoes temporary phase mixing due to the oscillations of stars at different frequencies, giving rise to phase spirals. These transients, however, are quickly taken over by long term oscillations driven at the forcing frequency Ω_{P}.

For a slowly growing spiral/bar, i.e., in the ‘adiabatic growth’ limit $(\gamma \to 0)$, the entire disk oscillates at the driving frequency, Ω_{P}, i.e.,

$$\mathcal{P}^{(j)}_{nlm}(t) \xrightarrow{\gamma_j \to 0} \exp\left[-im\Omega_{\mathrm{P}} t\right] \left[\pi\delta(\Omega_{\mathrm{res}}) - \frac{i}{\Omega_{\mathrm{res}}}\right]. \tag{35}$$

This has two major implications. First of all, since all stars, both resonant and non-resonant, are driven at the pattern speed of the perturbing spiral/bar, transient phase mixing does not occur and thus no phase spiral arises. Secondly, the response is dominated by the resonances, $\Omega_{\mathrm{res}} = 0$. In fact the resonant response diverges, reflecting the failure of (standard) linear perturbation theory near resonances. The adiabatic invariance of actions is partially broken near these resonances, causing the stars to get trapped in librating near-resonant orbits. A proper treatment of the near-resonant response can be performed by working with ‘slow’ and ‘fast’ action-angle variables (Tremaine & Weinberg 1984; Lichtenberg & Lieberman 1992; Chiba & Schönrich 2022; Banik & van den Bosch 2022; Hamilton et al. 2022), which are uniquely defined for each resonance as linear combinations of the original action-angle variables. The fast actions remain nearly invariant while the fast angles oscillate with periods comparable to the unperturbed orbital periods of stars. The slow action-angle variables, on the other hand, undergo large amplitude oscillations about their resonance values over a libration timescale that is typically much longer than the orbital periods. For example, at co-rotation resonance $(n = l = 0)$, angular momentum behaves as the slow action while the radial and vertical actions behave as the fast ones.

Based on the above discussion, we infer that phase spirals can only be excited in the galactic disk by transient spiral/bar perturbations whose amplitude changes over a timescale comparable to the vertical oscillation periods of stars. Persistent spirals or bars rotating with a fixed pattern speed cannot give rise to phase spirals. Rather they trigger stellar oscillations at the pattern speed itself, which manifests in the phase-space as a steadily rotating dipole or quadrupole depending on whether the $n = 1$ or 2 mode dominates the response. Thus, a phase spiral is necessarily always triggered by a transient perturbation.

4. DISK RESPONSE TO SATELLITE ENCOUNTER

In addition to the spiral arm/bar perturbations considered above, we also consider disk perturbations triggered by encounters with a satellite galaxy. For simplicity, we assume that the satellite is moving with uniform velocity v_{P} along a straight line, impacting the disk at a galactocentric distance R_{d} with an arbitrary orientation, specified by the angles, θ_{P} and ϕ_{P}, which are respectively defined as the angles between $\mathbf{v_P}$ and the z-axis, and between the projection of $\mathbf{v_P}$ on the mid-plane and the x-axis (see Fig. 2). Thus the position vector of the satellite with respect to the galactic center can be written as

$$\mathbf{r_P} = (R_{\mathrm{d}} + v_{\mathrm{P}} \sin\theta_{\mathrm{P}} \cos\phi_{\mathrm{P}}\, t)\, \hat{\mathbf{x}} + v_{\mathrm{P}} \sin\theta_{\mathrm{P}} \sin\phi_{\mathrm{P}}\, t\, \hat{\mathbf{y}} + v_{\mathrm{P}} \cos\theta_{\mathrm{P}}\, t\, \hat{\mathbf{z}}, \tag{36}$$

while that of a star is given by

$$\mathbf{r} = R(\cos\phi\, \hat{\mathbf{x}} + \sin\phi\, \hat{\mathbf{y}}) + z\, \hat{\mathbf{z}}. \tag{37}$$

We consider the satellite to be a Plummer sphere of mass M_{P} and size ε, such that its gravitational potential at location $\mathbf{r}$ is given by

$$\Phi_{\mathrm{P}} = -\frac{G M_{\mathrm{P}}}{\sqrt{\left|\mathbf{r} - \mathbf{r_P}\right|^2 + \varepsilon^2}}. \tag{38}$$

In order to compute the disk response to this external perturbation, we need to compute its Fourier coefficients, which is challenging. Rather, we first evaluate the τ-integral in Equation (22), setting $t_{\mathrm{i}} \to -\infty$, and then compute the Fourier transform of the result, as worked out in Appendix B.1. This yields

$$\begin{aligned} f_1(\mathbf{w}, \mathbf{I}, t) = &-\frac{2i}{\pi \sigma_R^2} \frac{1}{\sqrt{2\pi} h_z \sigma_z} \exp\left[-\frac{\kappa I_R}{\sigma_R^2}\right] \exp\left[-\frac{E_z(I_z)}{\sigma_z^2}\right] \Theta(L_z) \\ &\times \sum_{n,l,m=-\infty}^{\infty} \left[\left(\frac{n\Omega_z}{\sigma_z^2} + \frac{l\kappa}{\sigma_R^2}\right)\left(\frac{\Omega_\phi \Sigma}{\kappa}\right) - m \frac{\mathrm{d}}{\mathrm{d}L_z}\left(\frac{\Omega_\phi \Sigma}{\kappa}\right)\right] \mathcal{I}_{nlm}(\mathbf{I}, t)\, \exp\left[i\left(n w_z + l w_R + m w_\phi\right)\right], \end{aligned} \tag{39}$$

where $\mathcal{I}_{nlm}$ can be approximated for small I_R (this is justified since we adopt radial epicyclic approximation in this paper) as

$$\begin{aligned} \mathcal{I}_{nlm}(\mathbf{I}, t) \approx &-\frac{2GM_{\mathrm{P}}}{v_{\mathrm{P}}} \exp\left[-i\Omega t\right] \times \exp\left[-i\frac{\Omega \sin\theta_{\mathrm{P}} \cos\phi_{\mathrm{P}}}{v_{\mathrm{P}}} R_{\mathrm{d}}\right] \\ &\times \frac{1}{(2\pi)^2} \int_0^{2\pi} dw_z \exp\left[-i n w_z\right] \exp\left[i \frac{\Omega \cos\theta_{\mathrm{P}}}{v_{\mathrm{P}}} z\right] \int_0^{2\pi} d\phi\, \exp\left[-i m\phi\right] \exp\left[i \frac{\Omega \sin\theta_{\mathrm{P}} \cos\left(\phi - \phi_{\mathrm{P}}\right)}{v_{\mathrm{P}}} R_c\right] \\ &\times J_l\left(\frac{\Omega \sin\theta_{\mathrm{P}}}{v_{\mathrm{P}}} \sqrt{\frac{2I_R}{\kappa}} \cos\left(\phi - \phi_{\mathrm{P}}\right)\right) K_{0i}\left(\frac{\Omega \sqrt{\mathcal{R}_c^2 + \varepsilon^2}}{v_{\mathrm{P}}}, \frac{v_{\mathrm{P}} t - \mathcal{S}_c}{\sqrt{\mathcal{R}_c^2 + \varepsilon^2}}\right), \end{aligned} \tag{40}$$

with Ω given by

$$\Omega = n\Omega_z + l\kappa + m\Omega_\phi. \tag{41}$$

Here $\mathcal{R}_c = \mathcal{R}(R_c)$ and $\mathcal{S}_c = \mathcal{S}(R_c)$ with $\mathcal{R}$ and $\mathcal{S}$ given by equation (B14), and K_{0i} is given by equation (B16), which asymptotes to the modified Bessel function of the second kind, $K_0\left(\left|\Omega\right| \sqrt{\mathcal{R}_c^2 + \varepsilon^2}/v_{\mathrm{P}}\right)$, in the large time limit. A more precise expression for $\mathcal{I}_{nlm}$ that is valid for higher values of I_R is given by equation (B17) of Appendix B.1.

The expression for $\mathcal{I}_{nlm}$ given in equation (40) exhibits several key features of the disk response to satellite encounters. The $\exp\left[-i\Omega t\right]$ factor encodes the phase mixing of the response due to oscillations at different frequencies, giving rise

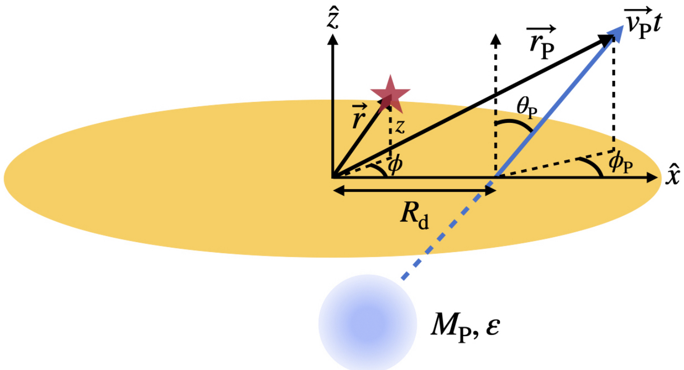

Figure 2: Illustration of the geometry of a satellite galaxy with mass $M_{\rm P}$ impacting a disk galaxy with uniform velocity $v_{\rm P}$ along a straight line. The impact occurs at a galactocentric distance $R_{\rm d}$. The orientation of $\mathbf{v_P}$ is specified by $\theta_{\rm P}$, the angle between $\mathbf{v_P}$ and the z-axis, and $\phi_{\rm P}$, the angle between the projection of $\mathbf{v_P}$ on the mid-plane and the x-axis.

to phase spirals. The $\exp\left[i\left(\Omega\cos\theta_{\rm P}/v_{\rm P}\right)z\right]$ and $\exp\left[i\left(\Omega\sin\theta_{\rm P}\cos\left(\phi-\phi_{\rm P}\right)/v_{\rm P}\right)R_c\right]$ factors respectively indicate that the satellite induces wave-like perturbations in the disk with two characteristic wave-numbers: the vertical wave-number, $k_z \approx \Omega\cos\theta_{\rm P}/v_{\rm P}$ and the horizontal wave-number, $k_R \approx \Omega\sin\theta_{\rm P}/v_{\rm P}$. Therefore, the disk response will be vertically (horizontally) stratified in case of a perpendicular (planar) impact of the satellite. As shown in Appendix B.2, expressions (39)-(40), which are complicated to compute, yield the correct response in the impulsive limit of a satellite having a face-on, perpendicular encounter through the center of the disk.

4.1. *Asymptotic behaviour of the response*

It is instructive to study the two extreme cases of encounter speed, the impulsive limit (large $v_{\rm P}$) and the adiabatic limit (small $v_{\rm P}$). Using the asymptotic forms of Bessel functions, we obtain the following approximate asymptotic behaviour of f_{1nlm}:

$$f_{1nlm} \sim \frac{GM_{\rm P}}{v_{\rm P}} \times \begin{cases} 1, & v_{\rm P} \to \infty \\ \\ \sqrt{v_{\rm P}/\Omega b}\,\exp\left[-\Omega b/v_{\rm P}\right], & v_{\rm P} \to 0, \end{cases} \tag{42}$$

where b is the impact parameter of the encounter, given by

$$b = \left|R_{\rm d} - R_c\right| \sqrt{1 - \sin^2\theta_{\rm P}\cos^2\phi_{\rm P}}. \tag{43}$$

It is clear from these limits that the disk response is most pronounced for intermediate velocities, $v_{\rm P} \sim \Omega b$. For impulsive encounters, the response is suppressed as a power law in $v_{\rm P}$, whereas in the adiabatic limit the response is exponentially suppressed, except at resonances, $\Omega = n\Omega_z + l\kappa + m\Omega_\phi = 0$. In this limit, far from the resonances, the perturbation timescale, $b/v_{\rm P}$, is much larger than Ω^{-1}, and the net response is washed away due to many oscillations during the perturbation (i.e., the actions are adiabatically invariant), a phenomenon known as adiabatic shielding (Weinberg 1994a,b; Gnedin & Ostriker 1999).

4.2. *Response of the MW disk to satellites*

The MW halo harbors several fairly massive satellite galaxies that perturbed the MW disk a few hundred Myr ago, thus triggering phase spirals that might have survived till the present day. Here we use existing data on the phase-space coordinates of the MW satellites to compute the disk response to their encounters with the MW stellar disk.

To compute the disk response to the MW satellites, we proceed as follows. As in Paper I, we adopt the galactocentric coordinates and velocities computed and documented by Riley et al. (2019) (table A.2, see also Li et al. 2020) and Vasiliev & Belokurov (2020) as initial conditions for the MW satellites. We then simulate their orbits in the combined gravitational potential of the MW halo, disk plus bulge[1] using a second order leap-frog integrator. For each individual orbit, we record the times, $t_{\rm cross}$, and the galactocentric radii, $R_{\rm d}$, corresponding to disk crossings. We also note the corresponding impact velocities, $v_{\rm P} = \sqrt{v_z^2 + v_R^2 + v_\phi^2}$, and the angles of impact, $\theta_{\rm P} = \cos^{-1}\left(v_z/v_{\rm P}\right)$ and $\phi_{\rm P} =$

[1] The bulge is modelled as a spherical Hernquist (1990) profile with mass $M_b = 6.5 \times 10^9\ {\rm M}_\odot$ and scale radius $r_b = 0.6$ kpc.

MW satellite name	Mass ($M_\odot$)	$f_{1,n=1}/f_0$	$t_{\rm cross}$ (Gyr)	$f_{1,n=1}/f_0$	$t_{\rm cross}$ (Gyr)	$f_{1,n=1}/f_0$	$t_{\rm cross}$ (Gyr)
		Penultimate	Penultimate	Last	Last	Next	Next
(1)	(2)	(3)	(4)	(5)	(6)	(7)	(8)
Sagittarius	10^9	2.8×10^{-1}	-1.01	4.9×10^{-8}	-0.35	1.3×10^{-1}	0.03
Hercules	7.1×10^6	8.4×10^{-8}	-3.78	2.4×10^{-3}	-0.5	2.3×10^{-3}	3.18
Leo II	8.2×10^6	–	-3.86	1.6×10^{-3}	-1.78	3.1×10^{-3}	2.31
Segue 2	5.5×10^5	6.2×10^{-4}	-0.84	8.5×10^{-4}	-0.25	6.3×10^{-5}	0.28
LMC	1.4×10^{11}	5.3×10^{-2}	-7.63	–	-2.67	2.3×10^{-2}	0.11
SMC	6.5×10^9	2.9×10^{-5}	-3.32	–	-1.44	9×10^{-6}	0.22
Draco I	2.2×10^7	–	-2.46	1×10^{-4}	-1.24	7×10^{-6}	0.24
Bootes I	10^7	1.7×10^{-7}	-1.67	3.8×10^{-5}	-0.35	–	0.88
Willman I	4×10^5	1.5×10^{-8}	-0.66	1.2×10^{-6}	-0.21	9×10^{-6}	0.41
Ursa Minor	2×10^7	–	-2.28	1.8×10^{-5}	-1.17	2.6×10^{-6}	0.29
Ursa Major II	4.9×10^6	5.5×10^{-6}	-2.12	2.6×10^{-6}	-0.09	–	0.97
Coma Berenices I	1.2×10^6	8.8×10^{-7}	-2.58	3.8×10^{-8}	-0.25	–	0.71
Sculptor	3.1×10^7	–	-2.74	3.2×10^{-8}	-0.46	–	1.48

Table 1: Response of the MW disk for stars with $I_z = h_{z\odot}\sigma_{z\odot}$ in the Solar neighborhood to encounters with satellites. Columns (1) and (2) list the name and dynamical mass of each satellite. The latter is taken from the literature (Simon & Geha 2007; Bekki & Stanimirović 2009; Łokas 2009; Erkal et al. 2019; Vasiliev & Belokurov 2020), except for Sagittarius for which we adopt a mass of 10^9 $M_\odot$. Note that there is a discrepancy between its estimated mass of $\sim 4 \times 10^8$ $M_\odot$ (Vasiliev & Belokurov 2020) and the mass required ($10^9 - 10^{10}$ $M_\odot$) to produce detectable phase spiral signatures in N-body simulations (see for example Bennett et al. 2022). Columns (3) and (4) respectively denote the bending mode response assuming our fiducial MW parameters and the penultimate disk-crossing time. Columns (5) and (6) indicate the same for the last disk-crossing, while columns (7) and (8) show it for the next one. Only satellites that induce a bending mode response, $f_{1,n=1}/f_0 \geq 10^{-8}$, in at least one of the three cases are shown. Any response weaker than 10^{-8} is considered negligible and is indicated with a horizontal dash.

$\tan^{-1}(v_\phi/v_R)$. We substitute these quantities in equation (B17) and compute the disk response marginalized over I_R using equation (39). Results are summarized in Table 1. Fig. 3 plots the amplitude of the Solar neighborhood ($R_c(L_z) = 8$kpc) bending mode response, $f_{1,n=1}/f_0$ (top panel), and breathing-to-bending ratio, $f_{1,n=2}/f_{1,n=1}$ (bottom panel), as a function of $t_{\rm cross}$. Here we only show the responses for $(l, m) = (0, 0)$ modes, and consider stars with $I_z = h_{z\odot}\sigma_{z\odot}$.

It is noteworthy that the responses in the realistic MW disk are $\sim 1 - 2$ orders of magnitude larger than those evaluated for the isothermal slab model shown in Fig. 7 of Paper I. This owes to the damping of the phase spiral amplitude due to lateral mixing, which is more pronounced in the isothermal slab with unconstrained lateral velocities than in the realistic disk with constrained, ordered motion. From the lower panel of Fig. 3 it is evident that, as in the isothermal slab case, almost all satellites trigger a bending mode response in the Solar neighborhood, resulting in a one-armed phase spiral in qualitative agreement with the Gaia snail. However, as is evident from the upper panel, only five of the satellites trigger a detectable response in the disk, with $f_{1,n=1}/f_0 > \delta = 10^{-4}$ (see Appendix C of Paper I for a derivation of this approximate detectability criterion for Gaia). The response to encounters with the other satellites is weak either because they have too low mass or because the encounter with respect to the Sun is too slow and adiabatically suppressed. Sgr excites the strongest response by far; its bending mode response, $f_{1,n=1}/f_0$, is at least $1 - 2$ orders of magnitude above that for any other satellite. Its penultimate disk crossing, about the same time as its last pericentric passage ~ 1 Gyr ago, triggered a strong response of $f_{1,n=1}/f_0 \sim 0.3$ in the Solar neighborhood. The response from its last disk crossing, which nearly coincides with its last apocentric passage about 350 Myr ago, triggered a very weak, adiabatically suppressed response that falls below the lower limit of Fig. 3. Its next disk crossing in about 30 Myr is estimated to trigger a strong response with $f_{1,n=1}/f_0 \sim 0.1$. Besides Sgr, the satellites that excite a detectable response, $f_{1,n=1}/f_0 > \delta = 10^{-4}$ are Hercules, Segue 2, Leo II and the LMC. The imminent crossing of LMC is estimated to trigger $f_{1,n=1}/f_0 \sim 2 \times 10^{-2}$, which is an order of magnitude below Sgr. Only for $I_z/(h_{z\odot}\sigma_{z\odot}) \gtrsim 4.5$ ($z_{\max} \gtrsim 3.4 h_{z\odot}$), the LMC response dominates over Sgr. This exercise therefore suggests

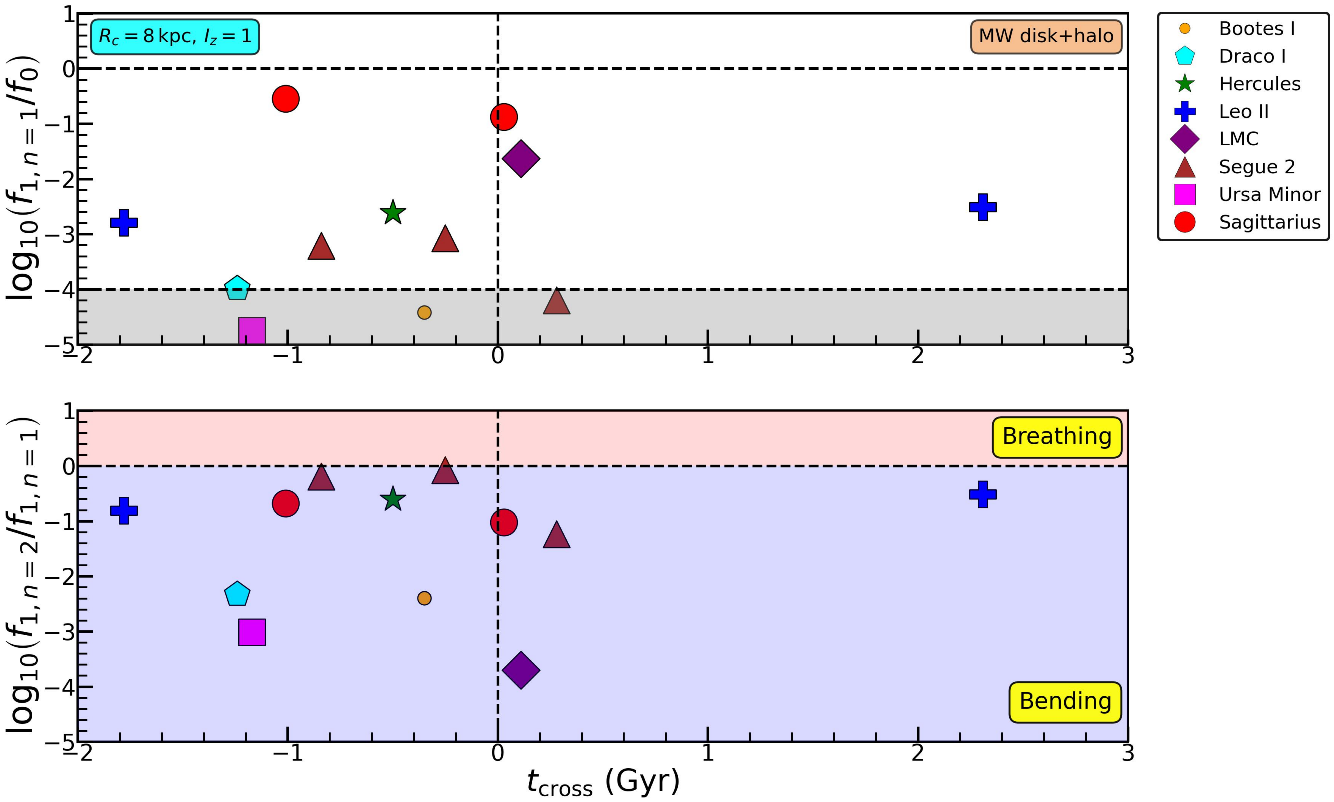

Figure 3: MW disk response to satellite encounter: bending mode strength, $f_{1,n=1}/f_0$ (upper panel), and the corresponding breathing vs bending ratio, $f_{1,n=2}/f_{1,n=1}$ (lower panel) for the $(l, m) = (0, 0)$ modes, in the Solar neighborhood for the MW satellites, as a function of the disk crossing time, $t_{\rm cross}$, in Gyr, where $t_{\rm cross} = 0$ marks today. The previous two and the next impacts are shown. Here we consider $I_z = h_z \sigma_{z\odot}$, with fiducial MW parameters, and marginalize over I_R. The effect of the (non-responsive) ambient DM halo on the stellar frequencies is taken into account. In the upper panel, the region with bending mode response, $f_{1,n=1}/f_0 < 10^{-4}$, has been grey-scaled, indicating that the response from the satellites in this region is far too weak and adiabatic to be detected by Gaia. Note that the response is dominated by that due to Sgr, followed by Hercules, Leo II, Segue 2 and the Large Magellanic Cloud (LMC). Also note that the previous two and next impacts of all the satellites excite bending modes in the Solar neighborhood.

that Sgr is the leading contender, among the MW satellites considered here, for triggering the Gaia snail in the Solar neighborhood, in agreement with several previous studies (Antoja et al. 2018; Binney & Schönrich 2018; Laporte et al. 2018, 2019; Darling & Widrow 2019a; Bland-Hawthorn et al. 2019; Hunt et al. 2021; Bland-Hawthorn & Tepper-García 2021; Bennett et al. 2022).

4.3. *Exploring parameter space*

Having computed the MW disk response to its satellites, we now investigate the sensitivity of the response to the various encounter parameters. In Fig. 4 we plot the amplitude of the Solar neighborhood response, $f_{1,nlm}/f_0$ (marginalized over I_R), as a function of the impact velocity, $v_{\rm P}$ (in units of the circular velocity at $R_c = R_\odot$), for the $(n, l, m) = (1, 0, 0)$ bending and $(n, l, m) = (2, 0, 0)$ breathing modes, shown in the left and right columns respectively. The top, middle and bottom rows show the results for varying I_z, $\theta_{\rm P}$ and $\phi_{\rm P}$ respectively, assuming the fiducial parameters to be those for Sgr (mass $M_{\rm P} = 10^9\,\mathrm{M}_\odot$, scale radius $\varepsilon = 1.6$ kpc) during its penultimate disk crossing (most relevant for the Gaia snail), i.e., impact radius $R_{\rm d} = 17$ kpc, impact velocity $v_{\rm P} = 340$ km/s, and angles of impact, $\theta_{\rm P} = 21^\circ$ and $\phi_{\rm P} = 150^\circ$. In Fig. 5 we plot the bending and breathing mode response amplitudes (in the Solar neighborhood) as a function of $v_{\rm P}$ for different (l, m) modes, with the fiducial parameters again corresponding to Sgr. The left and right columns respectively indicate the $n = 1$ bending and $n = 2$ breathing modes, while the top and

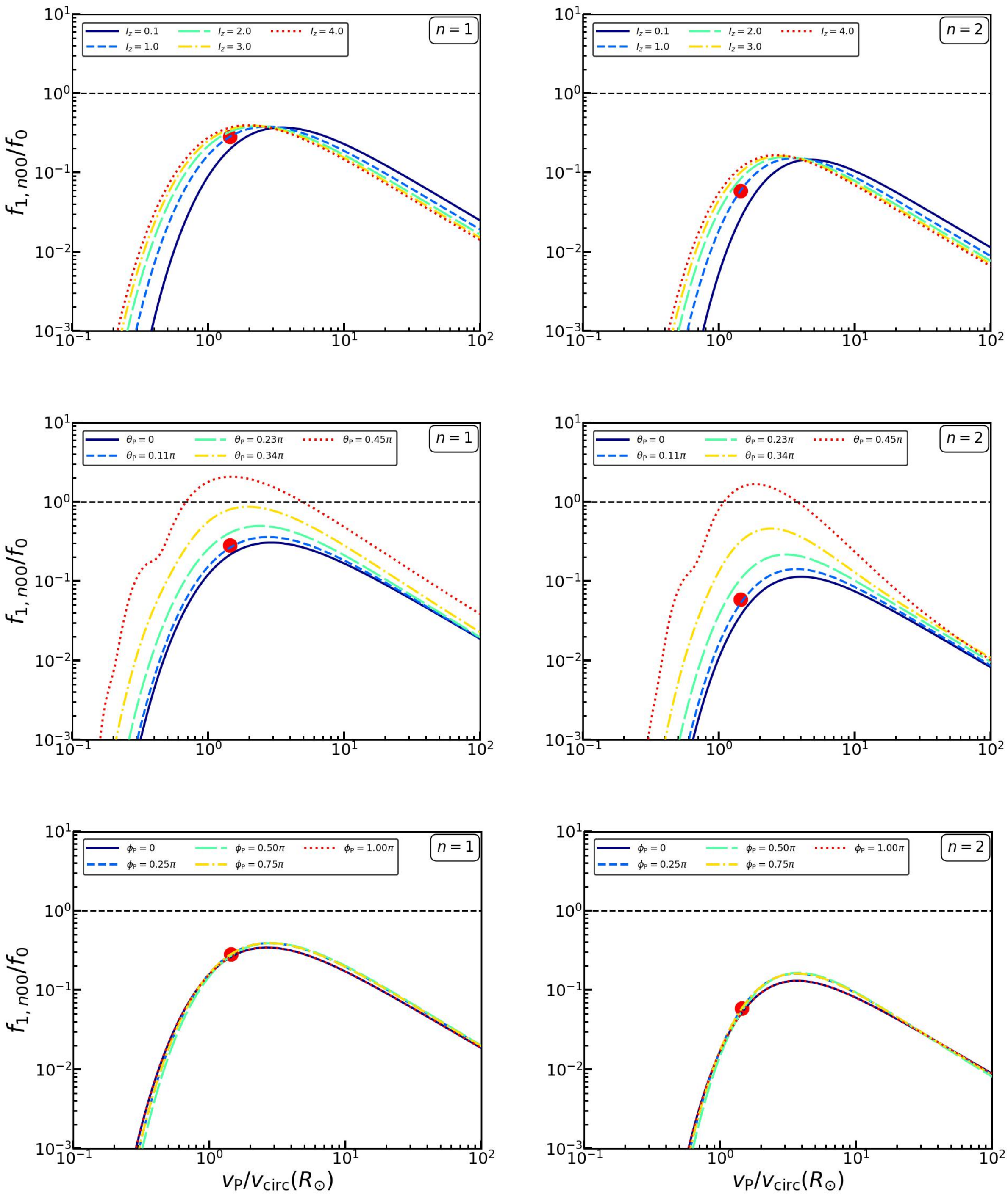

Figure 4: MW disk response to satellite encounter: each panel shows the behaviour of the disk response amplitude, $f_{1,n00}/f_0$ (evaluated using equations [39] and [B17]) and marginalized over I_R), as a function of the impact velocity, v_{P}, in the Solar neighborhood, i.e., $R_c = R_\odot = 8\,\mathrm{kpc}$, in presence of an ambient DM halo. The left and right columns respectively indicate the response for the $n = 1$ bending and $n = 2$ breathing modes. The top, middle and bottom rows show the same for different values of I_z (in units of $h_z\sigma_{z\odot}$), θ_{P} and ϕ_{P} respectively as indicated, with the fiducial parameters corresponding to $I_z = h_z\sigma_{z\odot}$ and the parameters for Sgr impact, the response amplitude for which is indicated by the red circle. Note that the response is suppressed as v_{P}^{-1} in the impulsive (large v_{P}) limit but exponentially suppressed in the adiabatic (small v_{P}) regime, and peaks at an intermediate velocity, $v_{\mathrm{P}} \sim 2{-}3\, v_{\mathrm{circ}}(R_\odot)$. The peak of the response shifts to smaller v_{P} for larger I_z due to a dip in Ω_z. The response is mildly dependent on ϕ_{P} but is quite sensitive to θ_{P}; more planar encounters, i.e., increasing θ_{P} triggers stronger responses.

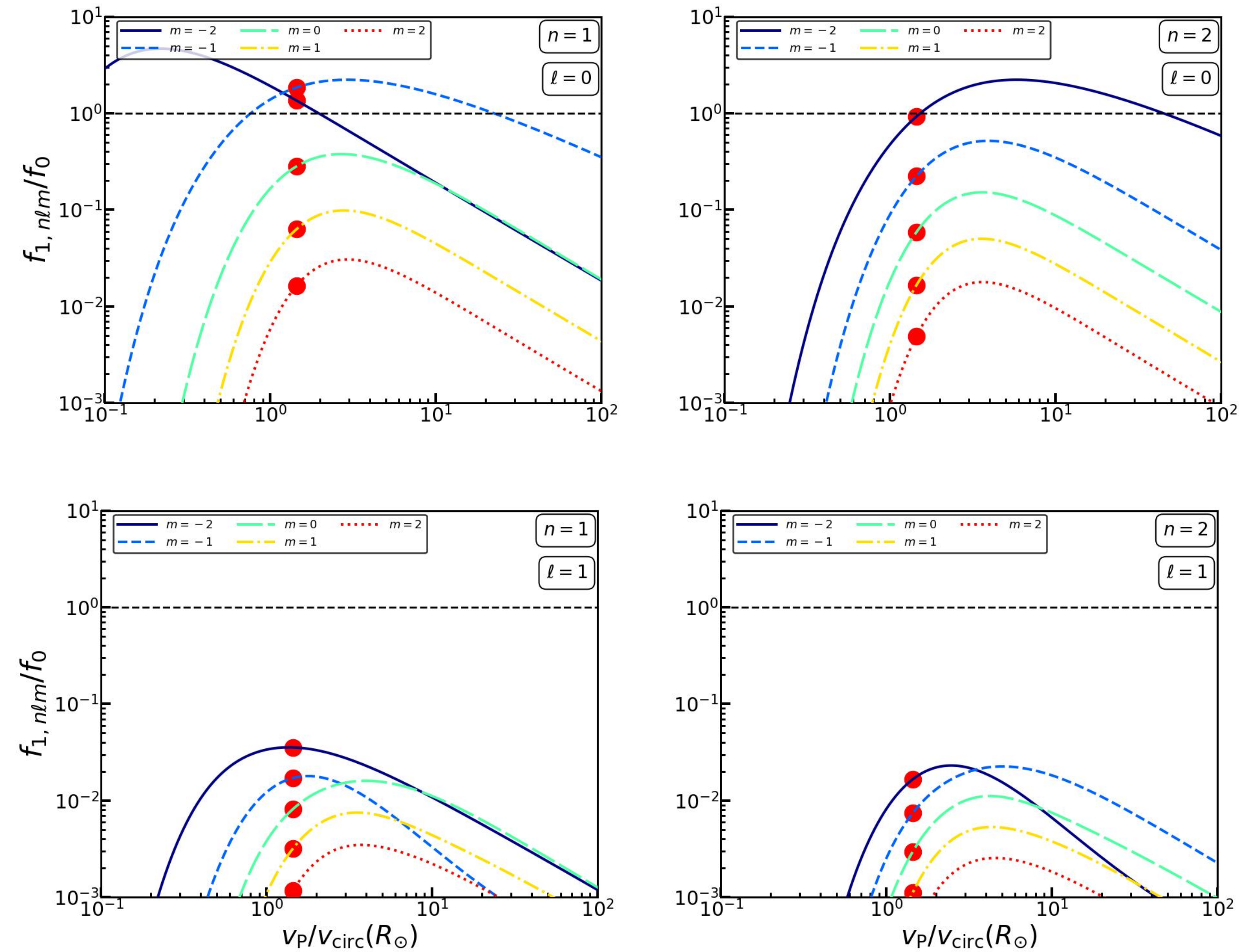

Figure 5: MW disk response to satellite encounter: each panel shows the behaviour of the disk response amplitude, $f_{1,nlm}/f_0$ (marginalized over I_R), as a function of the impact velocity, $v_{\rm P}$, in the Solar neighborhood, in presence of an ambient DM halo. Different lines correspond to different m modes as indicated. The top and bottom rows show the response for $l=0$ and 1 while the left and right columns indicate it for the $n=1$ bending and $n=2$ breathing modes. The fiducial parameters correspond to $I_z = h_z \sigma_{z\odot}$ and the parameters for Sgr impact, the response amplitudes for which are indicated by the red circles in each panel. The response is dominated by the $(n,l,m)=(1,0,-2)$ mode or the two-armed warp at small $v_{\rm P}$ and the $(2,0,-2)$ mode or the two-armed spiral at large $v_{\rm P}$. Typically, the $m=-2$ and -1 responses dominate over $m=0,1$ and 2, while the $l=0$ response is more pronounced than $l=1$.

bottom rows correspond to $l=1$ and $l=2$ respectively. The different lines in each panel denote the responses for $m=-2,-1,0,1$ and 2. Fig. 6 shows the ratio of the bending and breathing response amplitudes as a function of $v_{\rm P}$ for the dominant mode $(l,m)=(0,-2)$. Different lines indicate breathing-to-bending ratios for different values of $\theta_{\rm P}$, while the left and right columns respectively indicate the ratios observed at $R_c=8$ and 12 kpc.

From Figs. 4 and 5 it is evident that, as shown in equation (42), the disk response is suppressed like a power law ($\sim v_{\rm P}^{-1}$) in the high velocity/impulsive limit and exponentially ($\sim \exp\left[-\Omega b/v_{\rm P}\right]$) suppressed in the low velocity/adiabatic limit. The response is the strongest for intermediate velocities, $v_{\rm P} \sim 2-3\, v_{\rm circ}(\,R_\odot)$, where the time periods of the vertical, radial and azimuthal oscillations of the stars are nearly commensurate with the encounter timescale, $\sqrt{b^2+\varepsilon^2}/v_{\rm P}$. The $v_{\rm P}^{-1}$ and K_{0i} factors in equation (40) conspire to provide the near-resonance condition for maximum response,

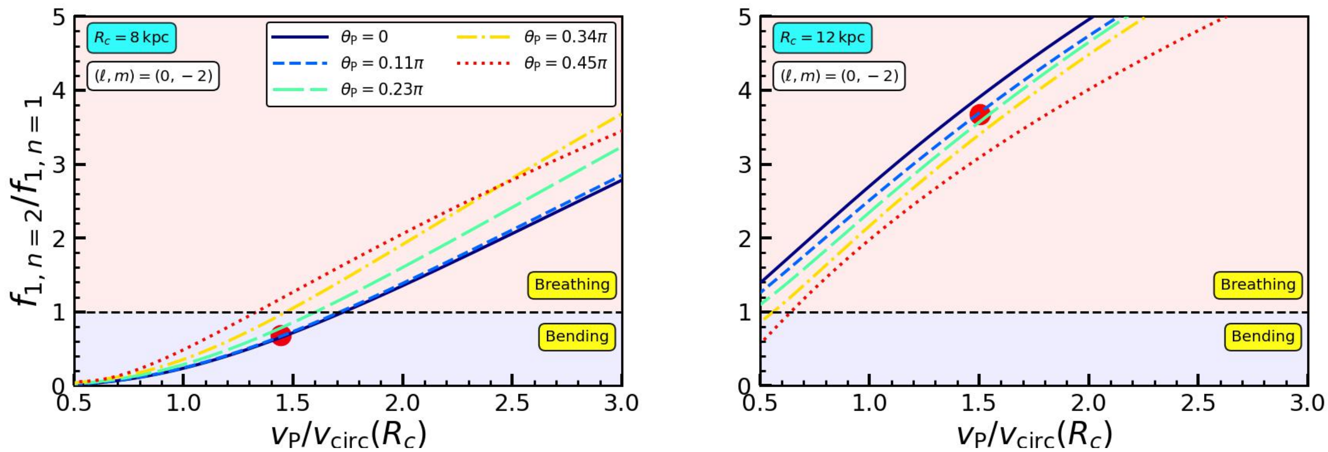

Figure 6: MW disk response to satellite encounter: breathing-to-bending ratio or the relative strength of the $n = 2$ and $n = 1$ modes of disk response to a Sgr-like impact is plotted as a function of the impact velocity, v_P, at $R_c = R_\odot = 8$kpc and $R_c = 1.5R_\odot = 12$kpc shown in the left and right columns respectively, for the $(l, m) = (0, -2)$ mode which typically dominates the response. Different lines correspond to different values of θ_P as indicated. We consider $I_z = h_z\sigma_{z\odot}$ and the fiducial parameters to correspond to those for Sgr encounter, for which the breathing-to-bending ratio is denoted by the red circle. Bending modes dominate over breathing modes at small v_P and vice versa at large v_P. Breathing modes are relatively more pronounced than bending modes in the outer disk, closer to the Sgr impact radius, $R_d = 17$ kpc. More planar (perpendicular) encounters trigger larger breathing-to-bending ratios farther away from (closer to) the impact radius.

$$n\Omega_z + l\kappa + m\Omega_\phi \approx \frac{0.6\, v_P}{\sqrt{b^2 + \varepsilon^2}}, \tag{44}$$

where b is the impact parameter of the encounter, given by equation (43). From the top panels of Fig. 4, it is clear that the peak response shifts to smaller v_P with increasing I_z since the corresponding vertical frequency, Ω_z, gets smaller making the encounter more impulsive for larger actions. The middle and bottom panels show that the response depends strongly on the polar angle of the encounter, θ_P, but very mildly on the azimuthal angle, ϕ_P. Moreover, the middle panels indicate that more planar encounters (larger θ_P) induce stronger responses.

The in-plane structure of the disk response depends on the relative contribution of the different (l, m) modes. From Fig. 5 it is evident that a typical Sgr-like encounter predominantly excites $(l, m) = (0, -1)$ and $(l, m) = (0, -2)$ in the Solar neighborhood. The dominant mode for slower encounters is $(n, l, m) = (1, 0, -2)$ while that for faster ones is $(n, l, m) = (2, 0, -2)$. Since $f_{1,nlm}/f_0 \gtrsim 1$ in these cases, the response to Sgr impact is in fact non-linear in the Solar neighborhood. Either way, a satellite encounter is typically found to excite strong $m = -2$ modes, i.e., 2-armed warps ($n = 1$) and spirals ($n = 2$). This owes its origin to a quadrupolar tidal distortion of the disk by the satellite, which manifests as a stretching of the disk in the direction of the impact and a squashing perpendicular to it.

Fig. 6 elucidates that the bending (breathing) mode response dominates for slower (faster) encounters, i.e., smaller (larger) v_P, and at guiding radii far from (close to) the impact radius, R_d. More planar impacts trigger larger breathing-to-bending ratios farther away from the impact radius while this trend reverses closer to it. This is because more planar (perpendicular) encounters cause more vertically symmetric perturbations farther away from (closer to) the impact radius. The predominance of bending modes for low v_P encounters while that of breathing modes for high v_P ones has been observed by Widrow et al. (2014) and Hunt et al. (2021) in their N-body simulations of satellite-disk encounters. As demonstrated by Widrow et al. (2014), slower encounters provide energy to the stars near one of the apocenters of vertical oscillations while drain energy from those near the other apocenter, thereby driving bending wave perturbations that are asymmetric about the mid-plane. On the other hand, fast satellite passages are impulsive and impart energy to the stars near both the apocenters, thus triggering symmetric breathing waves. The predominance of breathing (bending) modes closer to (farther away from) the impact radius is qualitatively similar to the observation by Hunt et al. (2021) in their simulations of MW-Sgr encounter that the outer part of the MW disk which is closer

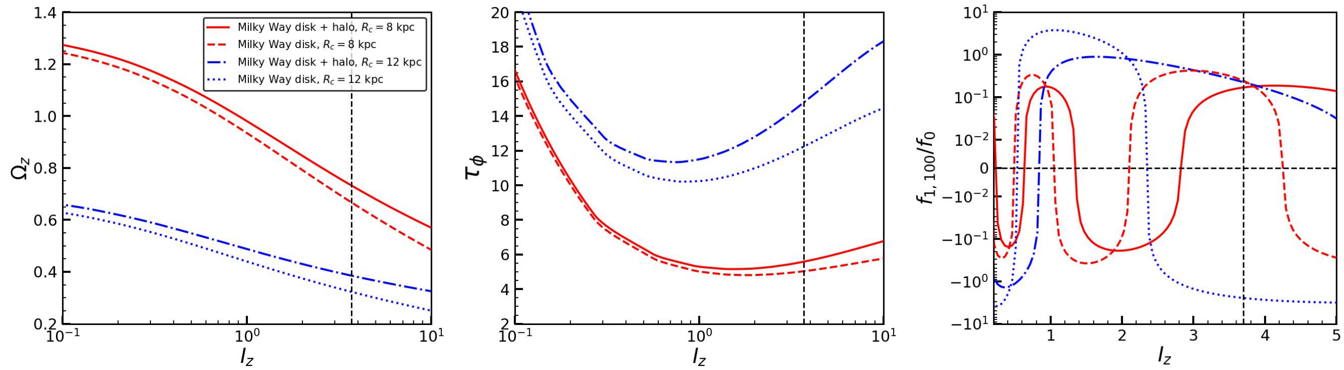

Figure 7: Impact of DM halo on vertical phase mixing: the panels from left to right respectively indicate the vertical frequency, Ω_z (units of σ_z/h_z), the vertical phase mixing timescale, τ_ϕ (given by equation [46]), and the $w_z = 0$ cuts of the phase spirals shown in Fig. 8 as a function of the vertical action, I_z (units of $h_z\sigma_z$). The solid and dashed red lines denote the cases with and without a halo for $R_c = R_\odot = 8\,\text{kpc}$ while the dot-dashed and dotted blue lines show the same for $R_c = 12\,\text{kpc}$. The vertical dashed line indicates roughly the maximum I_z for which a phase spiral is discernible in the Gaia data. Note that phase mixing occurs the fastest for $I_z \sim 1$ and that the inner disk phase mixes faster than the outer disk. Also note that the presence of a DM halo increases Ω_z as well as τ_ϕ, leading to slower phase mixing and therefore slower wrapping of the phase spiral. This effect is more pronounced in the outer disk.

to the impact radius shows a preponderance of two-armed phase spirals or breathing modes. This can be understood within the framework of our formalism by noting that the impact parameter, b, and therefore the encounter timescale $\sim \sqrt{b^2 + \varepsilon^2}/v_\mathrm{P}$ decreases with increasing proximity to the point of impact; hence the impact is faster than the vertical oscillations of stars near the point of impact, driving stronger breathing mode perturbations.

5. PHASE SPIRALS AS PROBES OF THE GALACTIC POTENTIAL

Thus far we mainly focused on how the nature of the perturbation dictates the vertical (i.e., bending and breathing modes) as well as the in-plane (various (l, m) modes) structure of the disk response. However, the detailed structure, in particular the winding, of the phase spiral not only depends on the triggering agent but also holds crucial information about the underlying potential in which the stars move, and can thus be used to constrain the potential of the combined disk plus halo system (see also Widmark et al. 2022a,b).

The winding of a phase spiral can be characterized by the pitch-angle, ϕ_I, along the ridge of maximum density. It is defined as the angle between the azimuthal direction and the tangent to the line of constant density (Binney & Tremaine 1987). It is related to the local dependence of the vertical frequency on the vertical action according to:

$$\phi_\mathrm{I} = \cot^{-1}\left[\left|I_z \frac{\mathrm{d}\Omega_z}{\mathrm{d}I_z}\right| t\right] = \cot^{-1}\left[\left|\frac{\mathrm{d}\Omega_z}{\mathrm{d}\ln I_z}\right| t\right]. \tag{45}$$

Following a perturbation, the pitch angle increases with time, asymptoting towards zero, as the spiral winds up as a consequence of the ongoing phase mixing. Based on the above expression for ϕ_I, we can define the following timescale of phase mixing,

$$\tau_\phi = \left|\frac{\mathrm{d}\ln I_z}{\mathrm{d}\Omega_z}\right|. \tag{46}$$

This timescale, which determines the rate of winding of the spiral, is a function of both the guiding radius, R_c, and the action, I_z, and is ultimately dictated by the (unperturbed) potential of the disk+halo system, which sets $\mathrm{d}\Omega_z/\mathrm{d}I_z$. Hence, the detailed shape of the phase spiral at a given location in the disk is sensitive to the local, relative strengths of the disk and halo, thereby opening up interesting avenues for constraining the detailed potential of the MW by examining phase spirals throughout the disk.

The left panel of Fig. 7 plots the vertical frequency, Ω_z, as a function of the logarithm of the action, I_z, for the MW potential with and without the halo and at guiding radii, $R_c = 8$ (red) and $12\,\text{kpc}$ (blue). The middle panel shows the behaviour of the corresponding phase mixing timescale, τ_ϕ, as a function of I_z. Fig. 8 shows the $(n, l, m) = (1, 0, 0)$

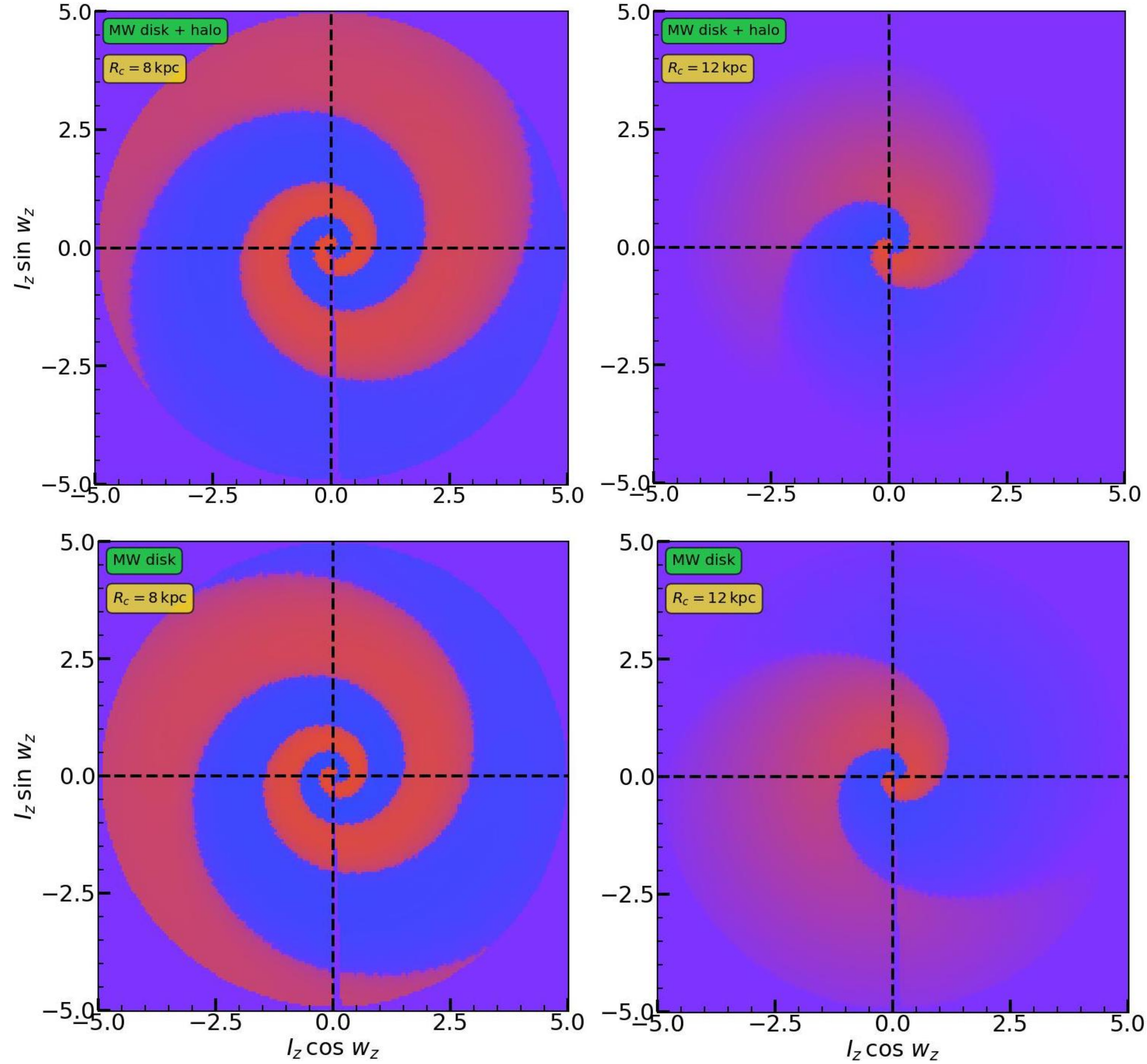

Figure 8: Vertical phase mixing: one-armed phase spiral corresponding to $n = 1$ bending mode excited by the encounter with Sgr for MW disk+halo and MW disk models (columns) at $R_c = 8\,\mathrm{kpc}$ and $12\,\mathrm{kpc}$ (rows). The presence of DM halo slows down the rate of phase mixing, leading to more loosely wrapped phase spirals. phase mixing occurs more rapidly in the inner disk than in the outer disk.

phase spirals 400 Myr after the penultimate disk crossing of Sagittarius, color coded by the MW disk response, $f_{1,100}$, with blue (red) indicating higher (lower) phase-space density. Results for the same four cases are shown as indicated. Finally, the right panel of Fig. 7 shows the $w_z = 0$ cuts of the normalized response, $f_{1,100}/f_0$, as a function of I_z, for the four different phase spirals. The vertical frequency, Ω_z, is a decreasing function of $\ln I_z$ in all cases, indicating that stars with larger actions (i.e., larger vertical excursion amplitudes) oscillate slower. Note that $|\mathrm{d}\Omega_z/\mathrm{d}\ln I_z|$ is an increasing (decreasing) function of I_z at small (large) I_z, reaching a maximum at intermediate I_z. Consequently, the phase mixing timescale, τ_ϕ, which is the inverse of $|\mathrm{d}\Omega_z/\mathrm{d}\ln I_z|$, attains its minimum at $I_z/(h_z\sigma_z) \sim 1$. Thus phase

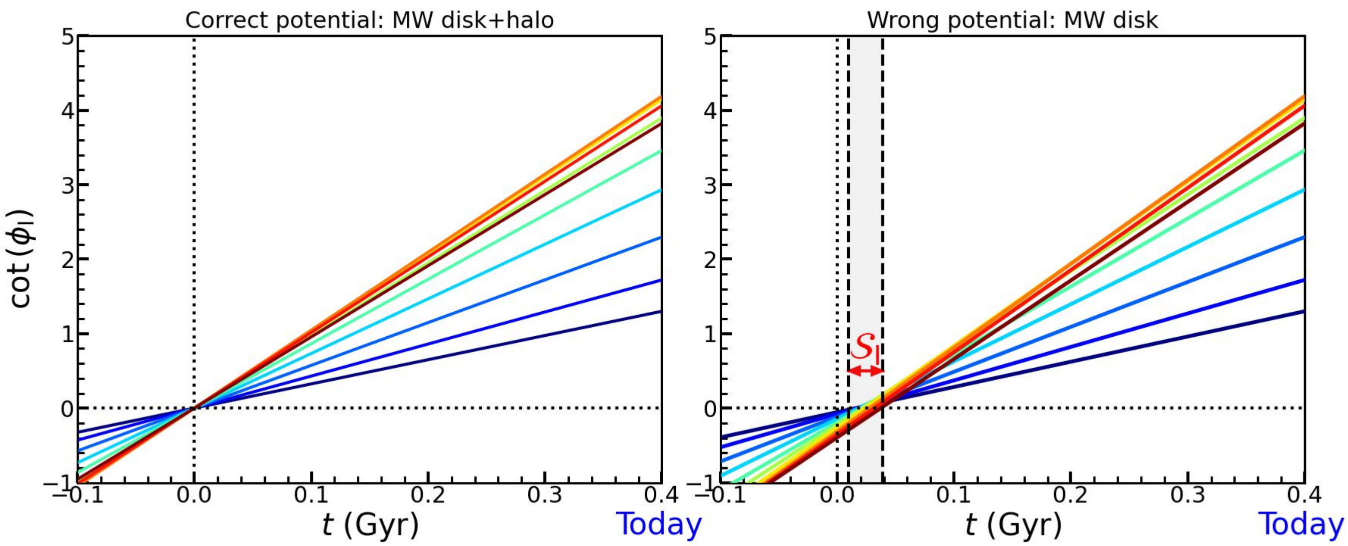

Figure 9: Unwinding the phase spiral and constraining the MW potential: Left panel plots the evolution of the cotangent of pitch-angle, ϕ_I, of a one-armed phase spiral as a function of time for different I_z, assuming that phase mixing occurs under the MW disk plus halo potential. Bluer (redder) colors indicate smaller (larger) I_z. Right panel plots the back-evolution of $\cot(\phi_\mathrm{I})$ from the present day measured values (0.4 Gyr since the perturbation occurred) assuming only the MW disk potential. Upon ignoring the halo and therefore assuming a 'wrong' potential, the different I_z lines intersect the $\cot(\phi_\mathrm{I}) = 0$ axis at different times, indicating the phase spiral is not perfectly unwound. One can therefore constrain the MW potential by iterating over the parameter space and trying to minimize the spread, $\mathcal{S}_\mathrm{I}$, in the intersection times.

mixing occurs the fastest at intermediate actions and slows down at larger actions, causing the spiral to become more loosely wound farther away from its origin.

The rate of phase mixing is different in the four different cases. Closer to the galactic center where the potential is deeper and steeper, stars have a larger range of Ω_z, or in other words Ω_z falls off more steeply with $\ln I_z$ in the inner disk than in the outskirts. This leads to faster phase mixing and therefore a much more tightly wound phase spiral in the inner disk (left panels of Fig. 8) as opposed to the outer disk (right panels). The difference in the phase mixing rates is also manifest in the $w_z = 0$ response shown in the right panel of Fig. 7; note the longer oscillation wavelengths of the blue lines (outer disk) as opposed to the red lines (inner disk). Hence, the inner part of the disk equilibrates much faster than the outer part.

The presence of a DM halo deepens the potential well and thus boosts the oscillation frequencies. But the halo also steepens the potential such that the range of frequencies is reduced, i.e., Ω_z falls off more mildly with $\ln I_z$ than in the disk only case. This leads to slower phase mixing and therefore more loosely wound phase spirals in presence of the halo (upper panels of Fig. 8) than in its absence (lower panels), the effect being more pronounced in the outer (right panels) than in the inner (left panels) disk. Equivalently, the $w_z = 0$ response in the right panel of Fig. 7 shows longer wavelength wiggles in presence of the halo.

The above sensitivity of the phase mixing timescale to the detailed galaxy potential can be used to constrain it. A proof of concept for this is demonstrated in Fig. 9. In the left panel we show how the cotangent of the pitch angle for a one-armed phase spiral in the Solar neighborhood changes as a function of time (equation [45]) due to the ongoing phase mixing of stars moving in the combined potential of the disk and halo of the MW. Different colors correspond to different vertical actions, I_z, with bluer (redder) colors indicating smaller (larger) I_z. Since τ_ϕ is a function of I_z, different actions undergo phase mixing at different rates indicated by the different slopes of the straight lines. Let us suppose that 400 Myr after the perturbation, an observer observes the phase spiral, i.e., measures the pitch angle, $\phi_\mathrm{I}(I_z)$ along the ridge of maximum density. They would now try to constrain the MW potential as well as the time elapsed since the perturbation by unwinding the phase spiral. This can be accomplished by making a prior guess of the potential and back-integrating the orbits of stars in this potential, i.e., back-evolving the pitch angle towards $\pi/2$ or $\cot\phi_\mathrm{I}$ towards zero. Only for the correct potential the pitch angle would return to $\pi/2$ for all actions at a single point of time in the past, or in other words the phase spiral would be perfectly unwound. In the right panel of Fig. 9 we demonstrate the result of this unwinding exercise for a slightly incorrect assumption of the MW potential where the halo is ignored. For this potential $\cot\phi_{\mathrm{I}}$ for different actions intersect the zero-line at different times. Therefore, the potential can be constrained by varying its parameters and trying to minimize the spread, $\mathcal{S}_{\mathrm{I}}$, of the intersection times of $\cot\phi_{\mathrm{I}}(I_z)$, as indicated. In future work we intend to implement this technique to unwind Gaia DR3 phase spirals at various locations of the MW disk and constrain the global potential and matter distribution of the MW.

6. CONCLUSION

In this paper, we have developed a linear perturbative formalism to analyze the response of a realistic disk galaxy (characterized by a pseudo-isothermal DF) embedded in an ambient spherical DM halo (modelled by an NFW profile) to perturbations of diverse spatiotemporal nature: bars, spiral arms, and encounters with satellite galaxies. Adopting the radial epicyclic approximation, we perturb the CBE up to linear order (in action-angle space) in presence of a perturbing potential, Φ_{P}, to compute the post-perturbation linear response in the DF, f_1, which shows oscillations at the unperturbed frequencies. Without self-gravity to reinforce the response, the oscillations phase mix away due to an intrinsic spread in the frequencies of stars, giving rise to spiral features in the phase-space distribution known as phase spirals. Depending on the timescale of Φ_{P}, different modes of disk oscillation, corresponding to different phase spiral structures, are excited. We summarize our conclusions as follows:

- Following an impulsive perturbation, the (n, l, m) mode of the disk response consists of stars oscillating with frequencies, $n\Omega_z$, $l\Omega_r \approx l\kappa$ and $m\Omega_\phi$, along vertical, radial and azimuthal directions respectively. Since the frequencies depend on the actions, primarily on the vertical action I_z and the angular momentum L_z, the response phase mixes away, spawning phase spirals. The dominant modes of vertical oscillation are the anti-symmetric bending ($n = 1$) and symmetric breathing ($n = 2$) modes, which induce initial dipolar and quadrupolar perturbations in the $z - v_z$ or $I_z \cos w_z - I_z \sin w_z$ phase-space that get phase-wrapped over time into one- and two-armed phase spirals respectively due to the variation of Ω_z with I_z.

- Since Ω_z and Ω_ϕ both depend on L_z, the amplitude of the $I_z \cos w_z - I_z \sin w_z$ phase spiral damps away over time, typically as $\sim 1/t$. Therefore, in a realistic disk with ordered motion, phase spirals damp out much slower due to lateral mixing than in the isothermal slab with unconstrained lateral velocities discussed in Paper I.

- The response to a bar or spiral arm with a fixed pattern speed, Ω_{P}, is dominated by the near-resonant stars ($\Omega_{\mathrm{res}} = n\Omega_z + l\kappa + m(\Omega_\phi - \Omega_{\mathrm{P}}) \approx 0$), especially in the adiabatic regime (slowly evolving perturber amplitude). The near-resonant response undergoes gradual phase mixing. Most of the strong resonances are confined to the disk-plane, such as the co-rotation ($n = l = 0$) and Lindblad ($n = 0, l = \pm 1, m = \pm 2$) resonances. For a transient bar or spiral arm whose amplitude varies over time as $\sim \exp\left[-\omega_0^2 t^2\right]$, the response from the non-resonant stars (Ω_{res} far from ω_0) undergoes phase mixing and is power-law (super-exponentially) suppressed in the impulsive (adiabatic) or $\omega_0 \gg \Omega_{\mathrm{res}}$ ($\omega_0 \ll \Omega_{\mathrm{res}}$) limit, reaching a maximum strength when $\Omega_{\mathrm{res}} \sim \omega_0$.

- For a thin disk, since Ω_z is very different from Ω_ϕ and κ, the vertical modes ($n \neq 0$) are generally not resonant with the radial and azimuthal ones and thus undergo phase mixing. The strength of a vertical mode primarily depends on the nature of the perturbing potential, most importantly its timescale. Slower pulses trigger stronger bending ($n = 1$) modes while faster pulses excite more pronounced breathing ($n = 2$) modes. Therefore, a transient bar or spiral arm with amplitude $\sim \exp\left[-\omega_0^2 t^2\right]$ triggers a bending (breathing) mode when the pulse-frequency, ω_0, is smaller (larger) than Ω_z. The response to very slow perturbations ($\omega_0 \ll \Omega_z$) is however heavily suppressed (adiabatic shielding).

- For a persistent bar or spiral arm with a fixed pattern speed, Ω_{P}, that grows and saturates over time, the phase spiral is a transient feature that is quickly taken over by coherent oscillations at the driving frequency, Ω_{P}, which manifest in the phase-space as a steadily rotating dipole (quadrupole) for the bending (breathing) mode. Therefore, a transient (pulse-like) perturbation, such as a bar or spiral arm whose amplitude varies over a timescale comparable to the vertical oscillation period, $T_z \sim h_z/\sigma_z$, is essential for the formation of a phase spiral.

- The above analysis suggests that if the recently discovered two-armed Gaia phase spiral (breathing mode) in the inner disk of the MW was indeed induced by spiral arms as suggested by Hunt et al. (2022) using N-body simulations, the spiral arm was probably a transient one with a predominantly symmetric vertical profile whose amplitude varied over a timescale shorter than the vertical oscillation period.

- We for the first time compute the full response of a disk galaxy embedded in a DM halo to a satellite galaxy (modelled as a Plummer perturber with mass M_{P} and size ε) moving along a straight line orbit with a uniform velocity, v_{P}, and impacting the disk at a galactocentric distance, R_{d}, at angles θ_{P} and ϕ_{P} (see Fig. 2). As an astrophysical application of this model we compute the response of our MW disk to several satellite galaxies in the halo. Our analysis shows that the Solar neighborhood response of the MW disk is dominated by Sgr, followed by the LMC, Hercules and Leo II. This makes Sgr the leading contender among the MW satellites for triggering the Gaia snail near the Solar radius.

- The amplitude of the response (at a fixed guiding radius R_c) to satellite encounters for all modes scales as v_{P}^{-1} in the impulsive (large v_{P}) limit, but is exponentially suppressed in the adiabatic (small v_{P}) limit, a phenomenon known as adiabatic shielding. The resonant modes with $n\Omega_z + l\kappa + m\Omega_\phi = 0$ are not suppressed but rather become non-linear in the adiabatic regime. The peak response of a mode (with $n\Omega_z + l\kappa + m\Omega_\phi \neq 0$) is achieved at intermediate velocities for which the encounter timescale is commensurate with the oscillation periods of the stars, i.e., the near-resonance condition,

$$n\Omega_z + l\kappa + m\Omega_\phi \approx \frac{0.6\, v_{\mathrm{P}}}{\sqrt{b^2 + \varepsilon^2}}, \tag{47}$$

is satisfied, with $b \approx |R_{\mathrm{d}} - R_c| \sqrt{1 - \sin^2\theta_{\mathrm{P}} \cos^2\phi_{\mathrm{P}}}$ the impact parameter.

- The response strength of a mode depends primarily on three parameters of satellite impact: 1. impact velocity v_{P}, 2. polar angle of impact θ_{P}, and 3. position on the disk relative to the point of impact. Slower, i.e., small v_{P} (faster, i.e., large v_{P}) encounters excite stronger $n = 1$ bending ($n = 2$ breathing) modes. More planar ($\theta_{\mathrm{P}} \approx \pi/2$) encounters result in stronger breathing-to-bending ratio farther away from the impact radius while this trend gets reversed closer to it. In general, breathing modes get stronger than bending modes closer to the impact radius, in agreement with the N-body simulations of MW-Sgr encounter performed by Hunt et al. (2021). Since the impact velocities of the MW satellites are not much different from the local circular velocity, the decisive factor for breathing *vs* bending modes is not the velocity but rather the distance of the observation radius from the impact radius.

- The $m = -2$ modes generally dominate the response for slower satellite encounters, e.g., that of Sgr with respect to the Solar neighborhood, due to the tidal distortion of the disk by the satellite. The in-plane spatial structure of the disk response therefore generally resembles a two-armed warp ($n = 1$) or spiral ($n = 2$).

- We investigate the impact of the MW potential on the shape of the phase spiral. We find that phase mixing occurs slower and thus phase spirals are more loosely bound farther out in the disk and in presence of a DM halo. We provide a proof-of-concept to use the tightness of the phase spiral, characterized by its pitch-angle, to constrain the MW potential, $\Phi_0(R, z)$. In future work we intend to apply this *spiral unwinding technique* to constrain $\Phi_0(R, z)$ using the Gaia data at various locations across the disk.

This paper is centered around the analysis of the phase mixing component (phase spirals) of the 'direct' disk response to various perturbations such as bars, spiral arms and satellite galaxies. However this leaves out some other potentially important features of the disk response. Firstly, we consider the ambient DM halo to non-responsive. In reality, the DM halo would also be perturbed, for example by an impacting satellite, and this halo response, which can be enhanced by self-gravity, can indirectly perturb the disk. Secondly, we have neglected the self-gravity of the disk response in this paper. As discussed in Paper I, the dominant effect of self-gravity would be coherent normal mode oscillations (Mathur 1990; Weinberg 1991; Darling & Widrow 2019b) of the disk which in linear theory are decoupled from the phase spirals. Recent developments (Dootson & Magorrian 2022) have shed some light into the self-gravitating response of razor-thin disks to bar perturbations. However, formulating a self-gravitating response theory for inhomogeneous thick disks and general perturber models (bars, spiral arms, satellite galaxies, etc.) is still an unsolved problem. We intend to include the effects of halo response and self-gravity on disk perturbations in future work.

ACKNOWLEDGMENTS

The authors are grateful to Kathryn Johnston, Jason Hunt, Adrian Price-Whelan, Chris Hamilton, Elena D'Onghia and Elise Darragh-Ford for insightful discussions and valuable suggestions. FCvdB is supported by the National Aeronautics and Space Administration through Grant No. 19-ATP19-0059 issued as part of the Astrophysics Theory Program. MDW is supported by the National Science Foundation through Grant No. AST-1812689.

REFERENCES

Antoja, T., Helmi, A., Romero-Gómez, M., et al. 2018, Nature, 561, 360, doi: 10.1038/s41586-018-0510-7

Banik, U., & van den Bosch, F. C. 2021a, ApJ, 912, 43, doi: 10.3847/1538-4357/abeb6d

—. 2021b, MNRAS, 502, 1441, doi: 10.1093/mnras/stab092

—. 2022, ApJ, 926, 215, doi: 10.3847/1538-4357/ac4242

Banik, U., Weinberg, M. D., & van den Bosch, F. C. 2022, ApJ, 935, 135, doi: 10.3847/1538-4357/ac7ff9

Bekki, K., & Stanimirović, S. 2009, MNRAS, 395, 342, doi: 10.1111/j.1365-2966.2009.14514.x

Bennett, M., Bovy, J., & Hunt, J. A. S. 2022, ApJ, 927, 131, doi: 10.3847/1538-4357/ac5021

Binney, J. 2010, MNRAS, 401, 2318, doi: 10.1111/j.1365-2966.2009.15845.x

Binney, J., & Schönrich, R. 2018, MNRAS, 481, 1501, doi: 10.1093/mnras/sty2378

Binney, J., & Tremaine, S. 1987, Galactic dynamics (Princeton University Press)

—. 2008, Galactic Dynamics: Second Edition (Princeton University Press)

Bland-Hawthorn, J., & Tepper-García, T. 2021, MNRAS, 504, 3168, doi: 10.1093/mnras/stab704

Bland-Hawthorn, J., Sharma, S., Tepper-Garcia, T., et al. 2019, MNRAS, 486, 1167, doi: 10.1093/mnras/stz217

Bovy, J. 2015, ApJS, 216, 29, doi: 10.1088/0067-0049/216/2/29

Bovy, J., & Rix, H.-W. 2013, ApJ, 779, 115, doi: 10.1088/0004-637X/779/2/115

Carlberg, R. G., & Sellwood, J. A. 1985, ApJ, 292, 79, doi: 10.1086/163134

Chiba, R., & Schönrich, R. 2022, MNRAS, 513, 768, doi: 10.1093/mnras/stac697

Darling, K., & Widrow, L. M. 2019a, MNRAS, 490, 114, doi: 10.1093/mnras/stz2539

—. 2019b, MNRAS, 484, 1050, doi: 10.1093/mnras/sty3508

Dootson, D., & Magorrian, J. 2022, arXiv e-prints, arXiv:2205.15725. https://arxiv.org/abs/2205.15725

Erkal, D., Belokurov, V., Laporte, C. F. P., et al. 2019, MNRAS, 487, 2685, doi: 10.1093/mnras/stz1371

Gaia Collaboration, Brown, A. G. A., Vallenari, A., et al. 2018, A&A, 616, A1, doi: 10.1051/0004-6361/201833051

Gandhi, S. S., Johnston, K. V., Hunt, J. A. S., et al. 2022, ApJ, 928, 80, doi: 10.3847/1538-4357/ac47f7

Gnedin, O. Y., & Ostriker, J. P. 1999, ApJ, 513, 626, doi: 10.1086/306864

Hamilton, C., Tolman, E. A., Arzamasskiy, L., & Duarte, V. N. 2022, arXiv e-prints, arXiv:2208.03855. https://arxiv.org/abs/2208.03855

Hernquist, L. 1990, ApJ, 356, 359, doi: 10.1086/168845

Hunt, J. A. S., Price-Whelan, A. M., Johnston, K. V., & Darragh-Ford, E. 2022, MNRAS, doi: 10.1093/mnrasl/slac082

Hunt, J. A. S., Stelea, I. A., Johnston, K. V., et al. 2021, MNRAS, 508, 1459, doi: 10.1093/mnras/stab2580

Johnston, K. V., Price-Whelan, A. M., Bergemann, M., et al. 2017, Galaxies, 5, 44, doi: 10.3390/galaxies5030044

Kaur, K., & Sridhar, S. 2018, ApJ, 868, 134, doi: 10.3847/1538-4357/aaeacf

Kaur, K., & Stone, N. C. 2022, MNRAS, 515, 407, doi: 10.1093/mnras/stac1729

Laporte, C. F. P., Johnston, K. V., Gómez, F. A., Garavito-Camargo, N., & Besla, G. 2018, MNRAS, 481, 286, doi: 10.1093/mnras/sty1574

Laporte, C. F. P., Minchev, I., Johnston, K. V., & Gómez, F. A. 2019, MNRAS, 485, 3134, doi: 10.1093/mnras/stz583

Li, H., & Widrow, L. M. 2021, MNRAS, 503, 1586, doi: 10.1093/mnras/stab574

Li, Z.-Y. 2021, ApJ, 911, 107, doi: 10.3847/1538-4357/abea17

Li, Z.-Z., Qian, Y.-Z., Han, J., et al. 2020, ApJ, 894, 10, doi: 10.3847/1538-4357/ab84f0

Lichtenberg, A., & Lieberman, M. 1992, Regular and Chaotic Dynamics

Łokas, E. L. 2009, MNRAS, 394, L102, doi: 10.1111/j.1745-3933.2009.00620.x

Lynden-Bell, D. 1962, MNRAS, 124, 279, doi: 10.1093/mnras/124.4.279

Lynden-Bell, D., & Kalnajs, A. J. 1972, MNRAS, 157, 1, doi: 10.1093/mnras/157.1.1

Maoz, E. 1991, ApJ, 375, 687, doi: 10.1086/170232

Mathur, S. D. 1990, MNRAS, 243, 529

McMillan, P. J. 2011, MNRAS, 414, 2446, doi: 10.1111/j.1365-2966.2011.18564.x

Miyamoto, M., & Nagai, R. 1975, PASJ, 27, 533

Navarro, J. F., Frenk, C. S., & White, S. D. M. 1997, ApJ, 490, 493, doi: 10.1086/304888

Price-Whelan, A., Sipőcz, B., Lenz, D., et al. 2020, adrn/gala: v1.3, v1.3, Zenodo, doi: 10.5281/zenodo.4159870

Price-Whelan, A. M. 2017, The Journal of Open Source Software, 2, doi: 10.21105/joss.00388

Riley, A. H., Fattahi, A., Pace, A. B., et al. 2019, MNRAS, 486, 2679, doi: 10.1093/mnras/stz973

Simon, J. D., & Geha, M. 2007, ApJ, 670, 313, doi: 10.1086/521816

Smith, R., Flynn, C., Candlish, G. N., Fellhauer, M., & Gibson, B. K. 2015, MNRAS, 448, 2934, doi: 10.1093/mnras/stv228

Sridhar, S. 1989, MNRAS, 238, 1159, doi: 10.1093/mnras/238.4.1159

Tremaine, S., & Weinberg, M. D. 1984, MNRAS, 209, 729, doi: 10.1093/mnras/209.4.729

van den Bosch, F. C., Ogiya, G., Hahn, O., & Burkert, A. 2018, MNRAS, 474, 3043, doi: 10.1093/mnras/stx2956

Vasiliev, E., & Belokurov, V. 2020, MNRAS, 497, 4162, doi: 10.1093/mnras/staa2114

Weinberg, M. D. 1989, MNRAS, 239, 549, doi: 10.1093/mnras/239.2.549

—. 1991, ApJ, 373, 391, doi: 10.1086/170059

—. 1994a, AJ, 108, 1398, doi: 10.1086/117161

—. 1994b, AJ, 108, 1403, doi: 10.1086/117162

—. 2004, arXiv e-prints, astro. https://arxiv.org/abs/astro-ph/0404169

Widmark, A., Hunt, J. A. S., Laporte, C. F. P., & Monari, G. 2022a, A&A, 663, A16, doi: 10.1051/0004-6361/202243173

Widmark, A., Laporte, C. F. P., & Monari, G. 2022b, A&A, 663, A15, doi: 10.1051/0004-6361/202142819

Widrow, L. M., Barber, J., Chequers, M. H., & Cheng, E. 2014, MNRAS, 440, 1971, doi: 10.1093/mnras/stu396

APPENDIX

A. FOURIER COEFFICIENTS OF SPIRAL ARM OR BAR PERTURBING POTENTIAL

An essential ingredient of the disk response to spiral arm or bar perturbations is the Fourier component of the perturber potential, Φ_{nlm}. This can be computed as follows:

$$\Phi_{nlm}(\mathbf{I},t) = \frac{1}{(2\pi)^3}\int_0^{2\pi} \mathrm{d}w_z \int_0^{2\pi} \mathrm{d}w_R \int_0^{2\pi} \mathrm{d}w_\phi \, \exp\left[-i(nw_z + lw_R + mw_\phi)\right] \Phi_{\mathrm{P}}\left(\mathbf{r},t\right). \tag{A1}$$

To evaluate this first we need to calculate $\mathbf{r} = (z, R, \phi)$ as a function of $(\mathbf{w}, \mathbf{I}) = (w_z, w_\phi, w_R, \mathbf{I})$ where $I_\phi = L_z$, the angular momentum. Under the epicyclic approximation, $w_\phi \approx \phi$, and R can be expressed as a sum of the guiding radius and an oscillating epicyclic term, i.e.,

$$R \approx R_c(L_z) + \sqrt{\frac{2I_R}{\kappa}}\sin w_R. \tag{A2}$$

The vertical distance z from the mid-plane is related to $R_c(L_z)$ and (w_z, I_z), according to

$$w_z = \Omega_z(R_c, I_z)\int_0^z \frac{\mathrm{d}z'}{\sqrt{2\left[E_z(R_c, I_z) - \Phi_z(R_c, z')\right]}}, \tag{A3}$$

where $\Omega_z(R_c, I_z) = 2\pi/T_z(R_c, I_z)$, with $T_z(R_c, I_z)$ given by Equation (20). The above equation can be numerically inverted to obtain $z(R_c, w_z, I_z)$.

Upon substituting the above expressions for R, ϕ and z in terms of $(\mathbf{w}, \mathbf{I})$ in the expression for Φ_{P} given in equation (23), we obtain

$$\begin{aligned}\Phi_{nlm}\left(\mathbf{I},t\right) = &-\frac{2\pi G\Sigma_{\mathrm{P}}}{k_R}\left(\sum_{m_\phi=0,2,-2}\delta_{m,m_\phi}\right)\frac{\mathrm{sgn}(m)\exp\left[i\,\mathrm{sgn}(m)k_R R_c(I_\phi)\right]}{2i} J_l\left(k_R\sqrt{\frac{2I_R}{\kappa}}\right)\\ &\times\left[\alpha\,\mathcal{M}_{\mathrm{o}}(t)\Phi_n^{(\mathrm{o})}(I_z) + \mathcal{M}_{\mathrm{e}}(t)\Phi_n^{(\mathrm{e})}(I_z)\right]\exp\left[-im\Omega_{\mathrm{P}}t\right],\end{aligned} \tag{A4}$$

where J_l is the l^{th} order Bessel function of the first kind,

$$\mathrm{sgn}(m) = \begin{cases}1, & m \geq 0,\\ -1, & m < 0,\end{cases} \tag{A5}$$

and $\Phi_n^{(\mathrm{o})}(I_z)$ and $\Phi_n^{(\mathrm{e})}(I_z)$ are given by

$$\begin{aligned}\Phi_n^{(\mathrm{o})}(I_z) &= \frac{1}{2\pi}\int_0^{2\pi}\mathrm{d}w_z\,\sin nw_z\,\mathcal{F}_{\mathrm{o}}\left(z, k_z^{(\mathrm{o})}\right),\\ \Phi_n^{(\mathrm{e})}(I_z) &= \frac{1}{2\pi}\int_0^{2\pi}\mathrm{d}w_z\,\cos nw_z\,\mathcal{F}_{\mathrm{e}}\left(z, k_z^{(\mathrm{e})}\right).\end{aligned} \tag{A6}$$

In deriving equation (A4) we have used the Hansen-Bessel formula which provides the following integral representation of Bessel functions of the first kind,

$$\int_0^{2\pi}\mathrm{d}x\,\exp\left[-ilx\right]\exp\left[i\alpha\sin x\right] = 2\pi J_l\left(\alpha\right) \tag{A7}$$

Using this we perform the w_R integral as follows:

$$\int_0^{2\pi}\mathrm{d}w_R\,\exp\left[-ilw_R\right]\exp\left[ik_R\sqrt{\frac{2I_R}{\kappa}}\sin w_R\right] = 2\pi J_l\left(k_R\sqrt{\frac{2I_R}{\kappa}}\right). \tag{A8}$$

We have also used the identity,

$$\int_0^{2\pi} \mathrm{d}\phi\, \exp\left[-im\phi\right] = 2\pi\, \delta_{m,0}. \tag{A9}$$

B. PERTURBATION BY ENCOUNTER WITH SATELLITE GALAXY

B.1. *Computation of the disk response*

To evaluate the disk response to satellite encounters using equation (22) we first evaluate the τ integral (with $t_{\mathrm{i}} \to -\infty$) of the satellite potential given in equation (38) and then compute the Fourier transform of the result. This yields the expression for the response in equation (39) with

$$\begin{aligned}
\mathcal{I}_{nlm}(\mathbf{I},t) &= \exp\left[-i\Omega t\right] \int_{-\infty}^{t} \mathrm{d}\tau\, \exp\left[i\Omega\tau\right] \Phi_{nlm}\left(\mathbf{I},\tau\right) \\
&= \frac{\exp\left[-i\Omega t\right]}{(2\pi)^3} \int_0^{2\pi} \mathrm{d}w_z \exp\left[-inw_z\right] \int_0^{2\pi} \mathrm{d}w_R \exp\left[-ilw_R\right] \int_0^{2\pi} \mathrm{d}w_\phi \exp\left[-imw_\phi\right] \int_{-\infty}^{t} \mathrm{d}\tau\, \exp\left[i\Omega\tau\right] \Phi_{\mathrm{P}}(z,R,\phi,\tau),
\end{aligned} \tag{B10}$$

where

$$\Omega = n\Omega_z + l\Omega_R + m\Omega_\phi. \tag{B11}$$

We perform the inner τ integral of Φ_{P} to obtain

$$\begin{aligned}
\int_{-\infty}^{t} \mathrm{d}\tau\, \exp\left[i\Omega\tau\right] \Phi_{\mathrm{P}}(z,R,\phi,\tau) &= -\frac{GM_{\mathrm{P}}}{v_{\mathrm{P}}} \exp\left[i\frac{\Omega\mathcal{S}}{v_{\mathrm{P}}}\right] \int_{-\infty}^{t-\mathcal{S}/v_{\mathrm{P}}} \mathrm{d}\tau \frac{\exp\left[i\Omega\tau\right]}{\sqrt{\tau^2 + (\mathcal{R}^2+\varepsilon^2)/v_{\mathrm{P}}^2}} \\
&= -\frac{GM_{\mathrm{P}}}{v_{\mathrm{P}}} \exp\left[i\frac{\Omega\mathcal{S}}{v_{\mathrm{P}}}\right] \int_{-\infty}^{(v_{\mathrm{P}}t-\mathcal{S})/\sqrt{\mathcal{R}^2+\varepsilon^2}} \mathrm{d}x \frac{\exp\left[i\left(\Omega\sqrt{\mathcal{R}^2+\varepsilon^2}/v_{\mathrm{P}}\right)x\right]}{\sqrt{x^2+1}} \\
&= -\frac{2\,GM_{\mathrm{P}}}{v_{\mathrm{P}}} \exp\left[i\frac{\Omega\mathcal{S}}{v_{\mathrm{P}}}\right] K_{0i}\left(\frac{\Omega\sqrt{\mathcal{R}^2+\varepsilon^2}}{v_{\mathrm{P}}}, \frac{v_{\mathrm{P}}t-\mathcal{S}}{\sqrt{\mathcal{R}^2+\varepsilon^2}}\right).
\end{aligned} \tag{B12}$$

Here K_{0i} is defined as

$$K_{0i}(\alpha,\beta) = \frac{1}{2}\int_{-\infty}^{\beta} \mathrm{d}x\, \frac{\exp\left[i\alpha x\right]}{\sqrt{x^2+1}}, \tag{B13}$$

which asymptotes to the zero-th order modified Bessel function of the second kind, $K_0\left(|\alpha|\right)$, in the limit $\beta \to \infty$. $\mathcal{R}$ and $\mathcal{S}$ are respectively the perpendicular and parallel projections along the direction of $\mathbf{v}_{\mathrm{P}}$ of the vector connecting the point of observation, (z,R,ϕ), with the point of impact, and are given by

$$\begin{aligned}
\mathcal{R}^2 &= \left[R\sin\left(\phi-\phi_{\mathrm{P}}\right) + R_{\mathrm{d}}\sin\phi_{\mathrm{P}}\right]^2 + \left[\left(R\cos\left(\phi-\phi_{\mathrm{P}}\right) - R_{\mathrm{d}}\cos\phi_{\mathrm{P}}\right)\cos\theta_{\mathrm{P}} - z\sin\theta_{\mathrm{P}}\right]^2 \\
\mathcal{S} &= \left(R\cos\left(\phi-\phi_{\mathrm{P}}\right) - R_{\mathrm{d}}\cos\phi_{\mathrm{P}}\right)\sin\theta_{\mathrm{P}} + z\cos\theta_{\mathrm{P}}.
\end{aligned} \tag{B14}$$

In the large time limit, i.e., $t \gg \mathcal{S}/v_{\mathrm{P}}$, K_{0i} asymptotes to $K_0\left(|\Omega|\sqrt{\mathcal{R}^2+\varepsilon^2}/v_{\mathrm{P}}\right)$. We substitute $\phi \approx w_\phi$ and the expressions for R and z in terms of $(\mathbf{w},\mathbf{I})$ given in equations (A2) and (A3) in the above expressions for $\mathcal{R}$ and $\mathcal{S}$. Further substituting the resultant τ integral from equation (B12) in equation (B10), adopting the small I_R limit and performing the w_R integral, we obtain

$$\begin{aligned}
\mathcal{I}_{nlm}(\mathbf{I},t) &\approx -\frac{2GM_{\mathrm{P}}}{v_{\mathrm{P}}} \exp\left[-i\Omega t\right] \times \exp\left[-i\frac{\Omega\sin\theta_{\mathrm{P}}\cos\phi_{\mathrm{P}}}{v_{\mathrm{P}}}R_{\mathrm{d}}\right] \\
&\times \frac{1}{(2\pi)^2} \int_0^{2\pi} dw_z \exp\left[-inw_z\right] \exp\left[i\frac{\Omega\cos\theta_{\mathrm{P}}}{v_{\mathrm{P}}}z\right] \int_0^{2\pi} d\phi\, \exp\left[-im\phi\right] \exp\left[i\frac{\Omega\sin\theta_{\mathrm{P}}\cos\left(\phi-\phi_{\mathrm{P}}\right)}{v_{\mathrm{P}}}R_c\right] \\
&\times J_l\left(\frac{\Omega\sin\theta_{\mathrm{P}}}{v_{\mathrm{P}}}\sqrt{\frac{2I_R}{\kappa}}\cos\left(\phi-\phi_{\mathrm{P}}\right)\right) K_{0i}\left(\frac{\Omega\sqrt{\mathcal{R}_c^2+\varepsilon^2}}{v_{\mathrm{P}}}, \frac{v_{\mathrm{P}}t-\mathcal{S}_c}{\sqrt{\mathcal{R}_c^2+\varepsilon^2}}\right),
\end{aligned} \tag{B15}$$

where $\mathcal{R}_c = \mathcal{R}(R = R_c)$ and $\mathcal{S}_c = \mathcal{S}(R = R_c)$. Here we have used the integral representation of Bessel functions of the first kind given in equation (A7) to compute the integral over w_R as follows:

$$\int_0^{2\pi} \mathrm{d}w_R \, \exp\left[-ilw_R\right] \exp\left[i\frac{\Omega \sin\theta_\mathrm{P}}{v_\mathrm{P}} \cos\left(\phi - \phi_\mathrm{P}\right)\sqrt{\frac{2I_R}{\kappa}} \sin w_R\right] = 2\pi J_l \left(\frac{\Omega \sin\theta_\mathrm{P}}{v_\mathrm{P}} \sqrt{\frac{2I_R}{\kappa}} \cos\left(\phi - \phi_\mathrm{P}\right)\right). \tag{B16}$$

The expression for $\mathcal{I}_{nlm}$ given in equation (B15) consists of the leading order expansion in $\sqrt{2I_R/\kappa}$. A more precise expression that is accurate up to second order in $\sqrt{2I_R/\kappa}$ is given, in the large time limit, as

$$\begin{aligned} \mathcal{I}_{nlm}(\mathbf{I}, t) \approx & -\frac{2GM_\mathrm{P}}{v_\mathrm{P}} \exp\left[-i\Omega t\right] \times \exp\left[-i\frac{\Omega \sin\theta_\mathrm{P} \cos\phi_\mathrm{P}}{v_\mathrm{P}} R_\mathrm{d}\right] \\ & \times \frac{1}{(2\pi)^2} \int_0^{2\pi} dw_z \exp\left[-inw_z\right] \exp\left[i\frac{\Omega\cos\theta_\mathrm{P}}{v_\mathrm{P}} z\right] \int_0^{2\pi} d\phi \, \exp\left[-im\phi\right] \, \exp\left[i\frac{\Omega \sin\theta_\mathrm{P} \cos\left(\phi - \phi_\mathrm{P}\right)}{v_\mathrm{P}} R_c\right] \\ & \times \left[\zeta^{(0)} J_l\left(\chi\right) - i\zeta^{(1)} J_l'\left(\chi\right) - \frac{1}{2}\zeta^{(2)} J_l''\left(\chi\right)\right], \end{aligned} \tag{B17}$$

where

$$\chi = \frac{\Omega \sin\theta_\mathrm{P}}{v_\mathrm{P}} \sqrt{\frac{2I_R}{\kappa}} \cos\left(\phi - \phi_\mathrm{P}\right), \tag{B18}$$

and

$$\begin{aligned} \zeta^{(0)} &= K_0\left(\eta\right), \\ \zeta^{(1)} &= \sqrt{\frac{2I_R}{\kappa}} \frac{\partial \mathcal{R}_c}{\partial R_c} \frac{\mathcal{R}_c}{\sqrt{\mathcal{R}_c^2 + \varepsilon^2}} \frac{|\Omega|}{v_\mathrm{P}} K_0'\left(\eta\right), \\ \zeta^{(2)} &= \frac{2I_R}{\kappa} \left[\left(\frac{\partial \mathcal{R}_c}{\partial R_c}\right)^2 \frac{\mathcal{R}_c^2}{\mathcal{R}_c^2 + \varepsilon^2} \frac{\Omega^2}{v_\mathrm{P}^2} K_0''(\eta) + \left\{\frac{\partial^2 \mathcal{R}_c}{\partial R_c^2} \frac{\mathcal{R}_c}{\mathcal{R}_c^2 + \varepsilon^2} + \left(\frac{\partial \mathcal{R}_c}{\partial R_c}\right)^2 \frac{\varepsilon^2}{\left(\mathcal{R}_c^2 + \varepsilon^2\right)^{3/2}}\right\} \frac{|\Omega|}{v_\mathrm{P}} K_0'(\eta)\right], \end{aligned} \tag{B19}$$

with

$$\eta = \frac{|\Omega| \sqrt{\mathcal{R}_c^2 + \varepsilon^2}}{v_\mathrm{P}}. \tag{B20}$$

Here each prime denotes a single derivative of the function with respect to its argument.

B.2. *Special case: disk response for face-on impulsive encounters*

The disk response in the general case, expressed by equation (40), depends on several encounter parameters: R_d, θ_P, ϕ_P, and is complicated to evaluate. Therefore, as a sanity check, here we compute the response as well as corresponding energy change for the special case of a satellite undergoing an impulsive, perpendicular passage through the center of the disk.

As shown in van den Bosch et al. (2018) (see also Banik & van den Bosch 2021b), the total energy change due to a head-on encounter of velocity v_P with a Plummer sphere of mass M_P and size ε is given by:

$$\Delta E = 4\pi \left(\frac{GM_\mathrm{p}}{v_\mathrm{P}}\right)^2 \int_0^\infty I_0^2(R)\Sigma(R)\frac{\mathrm{d}R}{R} \tag{B21}$$

where

$$I_0(R) = \int_1^\infty \frac{M_\mathrm{P}(\zeta R)}{M_\mathrm{p}} \frac{\mathrm{d}\zeta}{\zeta^2(\zeta^2-1)^{1/2}} \tag{B22}$$

Using that the enclosed mass profile of a Plummer sphere is given by $M_\mathrm{P}(R) = M_\mathrm{P} R^3 (R^2 + \varepsilon^2)^{-3/2}$, we have that $I_0(R) = R^2/(R^2 + \varepsilon^2)$, which yields

$$\Delta E = 4\pi \left(\frac{GM_\mathrm{p}}{v_\mathrm{P}}\right)^2 \int_0^\infty \Sigma(R) \frac{R^3 \mathrm{d}R}{(R^2+\varepsilon^2)^2}. \tag{B23}$$

Now we compute the disk response to the face-on satellite encounter using equations (39) and (B17-B20). For a perpendicular face-on impact through the center of the disk we have $R_{\rm d} = 0$ and $\theta_{\rm P} = 0$, implying that $\mathcal{R}_c$ becomes R_c. The corresponding response is greatly simplified. In the large time and small I_R limit, it is given by equation (39) with

$$\mathcal{I}_{nlm}(\mathbf{I},t) \approx -\frac{2GM_{\rm P}}{v_{\rm P}} \exp\left[-i\Omega t\right] \delta_{m,0} \times \frac{1}{2\pi} \int_0^{2\pi} dw_z \exp\left[-inw_z\right] \exp\left[i\frac{\Omega z}{v_{\rm P}}\right]$$
$$\times \frac{1}{2\pi} \int_0^{2\pi} {\rm d}w_R \, \exp\left[-ilw_R\right] K_0 \left[\frac{|\Omega|}{v_{\rm P}} \sqrt{\varepsilon^2 + \left(R_c + \sqrt{\frac{2I_R}{\kappa}} \sin w_R\right)^2}\right], \tag{B24}$$

where the ϕ integral only leaves contribution from the axisymmetric $m = 0$ mode. The w_R integrand can be expanded as a Taylor series and the w_R integral can be performed to yield the following leading order expression for $\mathcal{I}_{nlm}$:

$$\mathcal{I}_{nlm}(\mathbf{I},t) \approx i\frac{GM_{\rm P}}{v_{\rm P}} \exp\left[-i\Omega t\right] \delta_{m,0} \left(\delta_{l,1} - \delta_{l,-1}\right) \times \frac{1}{2\pi} \int_0^{2\pi} dw_z \exp\left[-inw_z\right] \exp\left[i\frac{\Omega z}{v_{\rm P}}\right]$$
$$\times \sqrt{\frac{2I_R}{\kappa}} \frac{R_c}{\sqrt{\varepsilon^2 + R_c^2}} \frac{|\Omega|}{v_{\rm P}} K_0' \left[\frac{|\Omega|}{v_{\rm P}} \sqrt{\varepsilon^2 + R_c^2}\right]. \tag{B25}$$

In the impulsive limit, $v_{\rm P} \to \infty$, this becomes

$$\mathcal{I}_{nlm}(\mathbf{I},t) \approx i \, \delta_{n,0} \delta_{m,0} \left(\delta_{l,1} - \delta_{l,-1}\right) \frac{GM_{\rm P}}{v_{\rm P}} \sqrt{\frac{2I_R}{\kappa}} \frac{R_c}{\varepsilon^2 + R_c^2} \exp\left[-i \, l\kappa \, t\right], \tag{B26}$$

which can be substituted in equation (22) to yield

$$f_{1nlm}\left(\mathbf{I},t\right) = f_0(\mathbf{I}) \times \delta_{n,0} \delta_{m,0} \left(\delta_{l,1} - \delta_{l,-1}\right) \frac{GM_{\rm P}}{v_{\rm P}} \frac{l\kappa}{\sigma_R^2} \sqrt{\frac{2I_R}{\kappa}} \frac{R_c}{\varepsilon^2 + R_c^2} \exp\left[-i \, l\kappa \, t\right], \tag{B27}$$

with f_0 given by equation (12). Hence, the response is given by

$$f_1\left(\mathbf{w},\mathbf{I},t\right) = \sum_{n=-\infty}^{\infty} \sum_{l=-\infty}^{\infty} \sum_{m=-\infty}^{\infty} \exp\left[i(nw_z + lw_R + mw_\phi)\right] f_{1nlm}(\mathbf{I},t)$$
$$= f_0(\mathbf{I}) \times \frac{2GM_{\rm P}}{v_{\rm P}} \frac{\sqrt{2\kappa I_R}}{\sigma_R^2} \frac{R_c}{\varepsilon^2 + R_c^2} \cos\left(w_R - \kappa t\right), \tag{B28}$$

which shows that the satellite passage introduces a relative overdensity, $f_1\left(\mathbf{w},\mathbf{I},t\right)/f_0(\mathbf{I})$, that scales as $\sim R_c/\left(\varepsilon^2 + R_c^2\right)$, which increases from zero at the center, peaks at $R_c = \varepsilon$, and asymptotes to zero again at large R_c. The $\cos(w_R - \kappa t)$-term describes the radial epicyclic oscillations in the response.

To compute the energy change due to the impact, we note that ${\rm d}E/{\rm d}t = \partial E/\partial\mathbf{I} \cdot {\rm d}\mathbf{I}/{\rm d}t$, where $\partial E/\partial\mathbf{I} = \mathbf{\Omega} = (\Omega_z, \Omega_R, \Omega_\phi)$ and ${\rm d}\mathbf{I}/{\rm d}t = \partial\Phi_{\rm P}/\partial\mathbf{w}$ from Hamilton's equations of motion. Thus the total phase-averaged energy injected per unit phase-space can be obtained as follows:

$$\left\langle \Delta E\left(\mathbf{I}\right)\right\rangle = \frac{1}{\left(2\pi\right)^3} \int {\rm d}\mathbf{w} \int_{-\infty}^{\infty} {\rm d}t \frac{{\rm d}E}{{\rm d}t} f_1(\mathbf{I},t) = \frac{1}{\left(2\pi\right)^3} \int {\rm d}\mathbf{w} \int_{-\infty}^{\infty} {\rm d}t \, \mathbf{\Omega} \cdot \frac{\partial\Phi_{\rm P}}{\partial\mathbf{w}} f_1(\mathbf{I},t). \tag{B29}$$

We can substitute the Fourier series expansions of $\Phi_{\rm P}$ and f_1 given in equations (8) in the above expression and integrate over $\mathbf{w}$ to obtain (Weinberg 1994a,b)

$$\left\langle \Delta E\left(\mathbf{I}\right)\right\rangle = i \sum_{nlm} \left(n\Omega_z + l\kappa + m\Omega_\phi\right) \int_{-\infty}^{\infty} {\rm d}t \, \Phi_{nlm}^*(\mathbf{I},t) f_{1nlm}(\mathbf{I},t). \tag{B30}$$

We can now substitute the form of Φ_{P} for a Plummer perturber given in equation (38), with $\mathbf{r_P}$ and $\mathbf{r}$ given by equations (36) and (37). The time integral can thus be written as

$$\int_{-\infty}^{\infty} \mathrm{d}t\, \Phi^{*}_{nlm}(\mathbf{I},t) f_{1nlm}(\mathbf{I},t) = -\frac{1}{(2\pi)^3} \int_0^{2\pi} \mathrm{d}w_z \exp\left[inw_z\right] \int_0^{2\pi} \mathrm{d}w_R \exp\left[ilw_R\right] \int_0^{2\pi} \mathrm{d}w_\phi \exp\left[imw_\phi\right]$$
$$\times \int_{-\infty}^{\infty} \mathrm{d}t \frac{GM_{\mathrm{P}}}{\sqrt{(v_{\mathrm{P}}t - z)^2 + R^2 + \varepsilon^2}} f_{1nlm}(\mathbf{I},t) \tag{B31}$$

Using equations (A2) and (A3) to express R and z in terms of $(\mathbf{w},\mathbf{I})$, and substituting the form for $f_{1nlm}(\mathbf{I},t)$ from equation (B27), we can perform the above integrals over $\mathbf{w}$ and t. Substituting the result in equation (B30) we obtain

$$\langle \Delta E\left(\mathbf{I}\right)\rangle = \left(\frac{GM_{\mathrm{P}}}{v_{\mathrm{P}}}\right)^2 f_0(\mathbf{I})\, \frac{2\kappa I_R}{\sigma_R^2}\, \frac{R_c^2}{\left(\varepsilon^2 + R_c^2\right)^2}. \tag{B32}$$

The total energy, ΔE_{tot}, imparted into the disk by the impulsive satellite passage can be computed by integrating the above expression over $\mathbf{I}$ and $\mathbf{w}$ (which simply introduces a factor of $(2\pi)^3$ since $\langle \Delta E\left(\mathbf{I}\right)\rangle$ is already phase-averaged), using equation (12) and transforming from L_z to R_c using the Jacobian $\mathrm{d}L_z/\mathrm{d}R_c = R_c\kappa^2/2\Omega_\phi$. This yields

$$\Delta E_{\mathrm{tot}} = 4\pi\left(\frac{GM_{\mathrm{P}}}{v_{\mathrm{P}}}\right)^2 \int_0^{\infty} \mathrm{d}R_c\, R_c\, \Sigma(R_c) \frac{R_c^2}{\left(\varepsilon^2 + R_c^2\right)^2}. \tag{B33}$$

This is indeed the expression for ΔE_{tot} derived under the impulse approximation given by equation (B23).